remote sensing

MDPI

Article

Long-Term Evaluation of GCOM-C/SGLI Reflectance and Water Quality Products: Variability Among JAXA G-Portal and JASMES

Salem Ibrahim Salem [1,2,*], Mitsuhiro Toratani [3], Hiroto Higa [4], SeungHyun Son [5,6], Eko Siswanto [7,8] and Joji Ishizaka [9]

[1] Faculty of Engineering, Kyoto University of Advanced Science, 18 Yamanouchi Gotanda-cho, Ukyo-ku, Kyoto 615-8577, Japan
[2] Faculty of Engineering, Alexandria University, Lotfy El-Sied st. off Gamal Abd El-Naser-Alexandria, Alexandria 11432, Egypt
[3] School of Architecture and Urban Planning, Tokai University, Kitakaname, Hiratsuka 259-1292, Japan; tora@tokai.ac.jp
[4] Institute of Urban Innovation, Yokohama National University, Hodogaya, Yokohama 240-8501, Japan; higa-h@ynu.ac.jp
[5] NOAA/NESDIS Center for Satellite Applications and Research, College Park, MD 20740, USA; seunghyun.son@noaa.gov
[6] Cooperative Institute for Satellite Earth System Studies (CISESS)/Earth System Science Interdisciplinary Center (ESSIC), University of Maryland, College Park, MD 20742, USA
[7] Earth Japan Agency for Marine-Earth Science and Technology (JAMSTEC), Showa-machi 3173-25, Yokohama 2360001, Japan; ekosiswanto@jamstec.go.jp
[8] Advanced Institute for Marine Ecosystem Change (AIMEC), Showa-machi 3173-25, Yokohama 2360001, Japan
[9] Institute for Space-Earth Environmental Research, Nagoya University, Furo-cho, Chikusa-ku, Nagoya 464-860, Japan; jishizaka@nagoya-u.jp
* Correspondence: salem.ibrahim@kuas.ac.jp or eng.salemsalem@gmail.com

Abstract: The Global Change Observation Mission-Climate (GCOM-C) satellite, launched in December 2017, is equipped with the Second-generation Global Imager (SGLI) sensor, featuring a moderate spatial resolution of 250 m and 19 spectral bands, including the unique 380 nm band. After six years in orbit, a comprehensive evaluation of SGLI products and their temporal consistency is needed. Remote sensing reflectance (R_{rs}) is the primary product for monitoring water quality, forming the basis for deriving key oceanic constituents such as chlorophyll-a (Chla) and total suspended matter (TSM). The Japan Aerospace Exploration Agency (JAXA) provides R_{rs} products through two platforms, G-Portal and JASMES, each employing different atmospheric correction methodologies and assumptions. This study aims to evaluate the SGLI full-resolution R_{rs} products from G-Portal and JASMES at regional scales (Japan and East Asia) and assess G-Portal R_{rs} products globally between January 2018 and December 2023. The evaluation employs in situ matchups from NASA's Aerosol Robotic Network-Ocean Color (AERONET-OC) and cruise measurements. We also assess the retrieval accuracy of two water quality indices, Chla and TSM. The AERONET-OC data analysis reveals that JASMES systematically underestimates R_{rs} values at shorter wavelengths, particularly at 412 nm. While the R_{rs} accuracy at 412 nm is relatively low, G-Portal's R_{rs} products perform better than JASMES at shorter wavelengths, showing lower errors and stronger correlations with AERONET-OC data. Both G-Portal and JASMES show lower agreement with AERONET-OC and cruise datasets at shorter wavelengths but demonstrate improved agreement at longer wavelengths (530 nm, 565 nm, and 670 nm). JASMES generates approximately 12% more matchup data points than G-Portal, likely due to G-Portal's stricter atmospheric correction thresholds that exclude pixels with high reflectance. In situ measurements indicate that G-Portal provides better overall agreement, particularly at lower R_{rs} magnitudes and Chla concentrations below 5 mg/m^3. This evaluation underscores the complexities and challenges of atmospheric correction, particularly in optically complex coastal waters (Case 2 waters), which may require tailored

Academic Editors: Chung-Ru Ho, Po-Chun Hsu, Shota Katsura, Bingqing Liu and Jen-Ping Peng

Received: 19 September 2024
Revised: 18 December 2024
Accepted: 20 December 2024
Published: 9 January 2025

Citation: Salem, S.I.; Toratani, M.; Higa, H.; Son, S.; Siswanto, E.; Ishizaka, J. Long-Term Evaluation of GCOM-C/SGLI Reflectance and Water Quality Products: Variability Among JAXA G-Portal and JASMES. *Remote Sens.* **2025**, *17*, 221. https://doi.org/10.3390/rs17020221

atmospheric correction methods different from the standard approach. The assessment of temporal consistency and seasonal variations in R_{rs} data shows that both platforms effectively capture interannual trends and maintain temporal stability, particularly from the 490 nm band onward, underscoring the potential of SGLI data for long-term monitoring of coastal and oceanic environments.

Keywords: AERONET; atmospheric correction; calibration; GCOM-C; NASA SeaBASS; ocean color

1. Introduction

Ocean color refers to the observed color of a waterbody, which is determined by the interaction of light with water itself and its constituents, including phytoplankton, non-algal particles, and dissolved organic matter [1,2]. This color is quantified in several forms, primarily through normalized water-leaving radiance ($nL_W(\lambda)$), remote sensing reflectance ($R_{rs}(\lambda)$), and water-leaving reflectance ($\rho_W(\lambda)$) [3,4]. $nL_W(\lambda)$ provides a normalized measure of the radiance exiting the water surface, while $R_{rs}(\lambda)$ relates the radiance to the extraterrestrial solar irradiance (F_0, [5]) using the formula $R_{rs}(\lambda) = nL_W/F_0$ [5]. $\rho_W(\lambda)$ is derived as $\pi R_{rs}(\lambda)$. Beyond deriving geophysical variables like chlorophyll-a (Chla) [6–9] and inherent optical properties (IOPs) like absorption and backscattering coefficients [10,11], ocean color is essential for monitoring environmental threats that pose significant ecological and public health risks, including harmful algal blooms [12] and blue tides [13].

While ocean color can be measured directly in the field, satellite observations offer the advantage of comprehensive global-scale monitoring of oceanic, coastal, and inland water bodies. The spatial and temporal coverage provided by satellite data is unparalleled, allowing for continuous monitoring and large-scale environmental assessments that are not feasible through in situ measurements alone. Among the various ocean color missions, the Global Change Observation Mission-Climate (GCOM-C) carrying the Second-generation Global Imager (SGLI) stands out due to its unique capabilities [14]. The GCOM-C/SGLI mission features a 380 nm band, which aids in improved detection of atmospheric aerosols and water constituents [15]. For instance, the absorption of colored dissolved organic matter (aCDOM) often predominates the inherent light absorption at ultraviolet (UV) and blue wavelengths in coastal waters [16,17]. Therefore, utilizing the UV band might reduce uncertainties associated with extracting aCDOM from blue bands, where its absorbance spectra frequently overlap with phytoplankton [18]. Additionally, SGLI offers a spatial resolution of 250 m, providing finer detail compared to other common ocean color sensors like Visible Infrared Imaging Radiometer Suite (VIIRS) and Moderate Resolution Imaging Spectroradiometer (MODIS) of 750 m and 1 km, respectively [19,20]. This improved resolution allows for better monitoring of coastal and inland water bodies where spatial heterogeneity is significant [21].

Satellites measure the radiance at the top of the atmosphere (TOA), which includes contributions from multiple sources, like Rayleigh scattering by gas molecules, aerosol scattering, sun-glint from the water surface, reflectance from whitecaps and foam, and water-leaving radiance [22]. The atmospheric gases and aerosols often represent 80% or more of the total signal observed at the TOA [23–25]. This significant atmospheric contribution makes it challenging to separate the water-leaving radiance from the TOA signal, particularly in the UV and blue regions [26]. Furthermore, variability in aerosol properties and distributions, as well as dynamic changes in sun-glint and whitecaps, add complexity to the atmospheric correction process [27].

Japan Aerospace Exploration Agency (JAXA) distributes SGLI data through the G-Portal and JASMES platforms. The atmospheric correction methods applied by the G-Portal [28] and JASMES [29] differ in their methodologies, assumptions, and the sequence of processes. Additionally, each atmospheric correction scheme incorporates unique features not present in the other; for instance, G-Portal includes a high-reflectance correction approach that is not implemented in JASMES. These differences underscore the importance of evaluating R_{rs} products to ensure their accuracy and reliability, which are vital for various oceanographic and climate studies.

While R_{rs} products are crucial for monitoring water bodies, they do not offer a direct assessment of water quality. Therefore, researchers often turn to other water quality indicators such as Chla and total suspended matter (TSM) to better depict environmental conditions. Chla is commonly used to assess phytoplankton biomass, serving as a key indicator of phytoplankton abundance and nutrient levels in aquatic environments [30–32]. TSM provides information on the concentration of suspended particles, which influences water clarity and light penetration, thereby affecting aquatic ecosystems [33,34]. Accurate retrieval of these products from R_{rs} data is vital for effectively monitoring and managing aquatic ecosystems, especially in coastal and inland waters where human activities and natural processes significantly impact water quality.

No research has yet comprehensively evaluated and compared the R_{rs} products from both G-Portal and JASMES. This study aims to fill that gap by assessing the R_{rs} products from both platforms at regional scales (Japan and East Asia) while extending the evaluation of G-Portal products globally. The assessment utilizes in situ measurements from field campaigns and NASA's Aerosol Robotic Network-Ocean Color (AERONET-OC) network [35–37], covering both Japan and a global scale. We will examine these products' accuracy and interannual variability over six years (January 2018–December 2023). Additionally, we will evaluate key water quality indices—Chla and TSM—against in situ measurements to determine their reliability. Finally, this study will investigate the agreement between JAXA's G-Portal and JASMES R_{rs} and water quality products, particularly over Japan. This evaluation is essential for enhancing the application of SGLI data in monitoring and managing marine and coastal environments.

2. Methods

2.1. GCOM-C/SGLI Characteristics

The GCOM-C satellite was developed to monitor global environmental changes, such as climate change, ocean color, vegetation indexes, and aerosols. It features the SGLI sensor, designed to succeed the Global Imager (GLI) mounted on the ADEOS-II satellite.

SGLI includes polarized and non-polarized observation capabilities and features two main components: the Visible and Near Infrared Radiometer (SGLI-VNR) and the Infrared Scanner (SGLI-IRS). It operates with a swath width of 1150 km for SGLI-VNR and 1400 km for SGLI-IRS. SGLI spans a wide spectral range from the UV to the thermal infrared (380 nm to 12 μm) across 19 bands, including 7 bands in the UV–visible range (380, 412, 443, 490, 530, 565, 670 nm). The spatial resolution of SGLI ranges from 250 m to 1 km (Table A1), with near-global coverage within approximately two days. This extensive coverage and high spatial and temporal resolution enable SGLI to capture dynamic environmental processes.

2.2. G-Portal and JASMES Platforms

JAXA provides GCOM-C/SGLI through two platforms: G-Portal and JASMES. G-Portal (Global Portal, https://gportal.jaxa.jp/gpr/, accessed on 15 January 2024) is an online platform designed to provide comprehensive access to a wide range of remote

sensing data. It offers a user-friendly interface to search, view, and download various types of Earth observation data, including the standard products of GCOM-C/SGLI.

In addition to G-Portal, JAXA has developed the JAXA Satellite Monitoring for Environmental Studies (JASMES, https://www.eorc.jaxa.jp/JASMES/, accessed on 15 January 2024) platform, which processed and analyzed data products derived from multiple satellite missions, including GCOM-C/SGLI. This platform offers a range of data products, such as vegetation indices, ocean color, atmospheric parameters, and other environmental indicators, to support research and applications in climate change, ecosystem monitoring, and disaster management.

G-Portal offers R_{rs} products at different resolutions: full resolution (250 m) and reduced resolution (1 km), both available globally. JASMES provides near-real-time (NRT) SGLI R_{rs} products (https://www.eorc.jaxa.jp/JASMES/SGLI_NRT/, accessed on 15 January 2024) with a 250 m spatial resolution over Japan (20–30°N and 115–155°E, the dashed box in Figure 1a) and a 5 km spatial resolution globally.

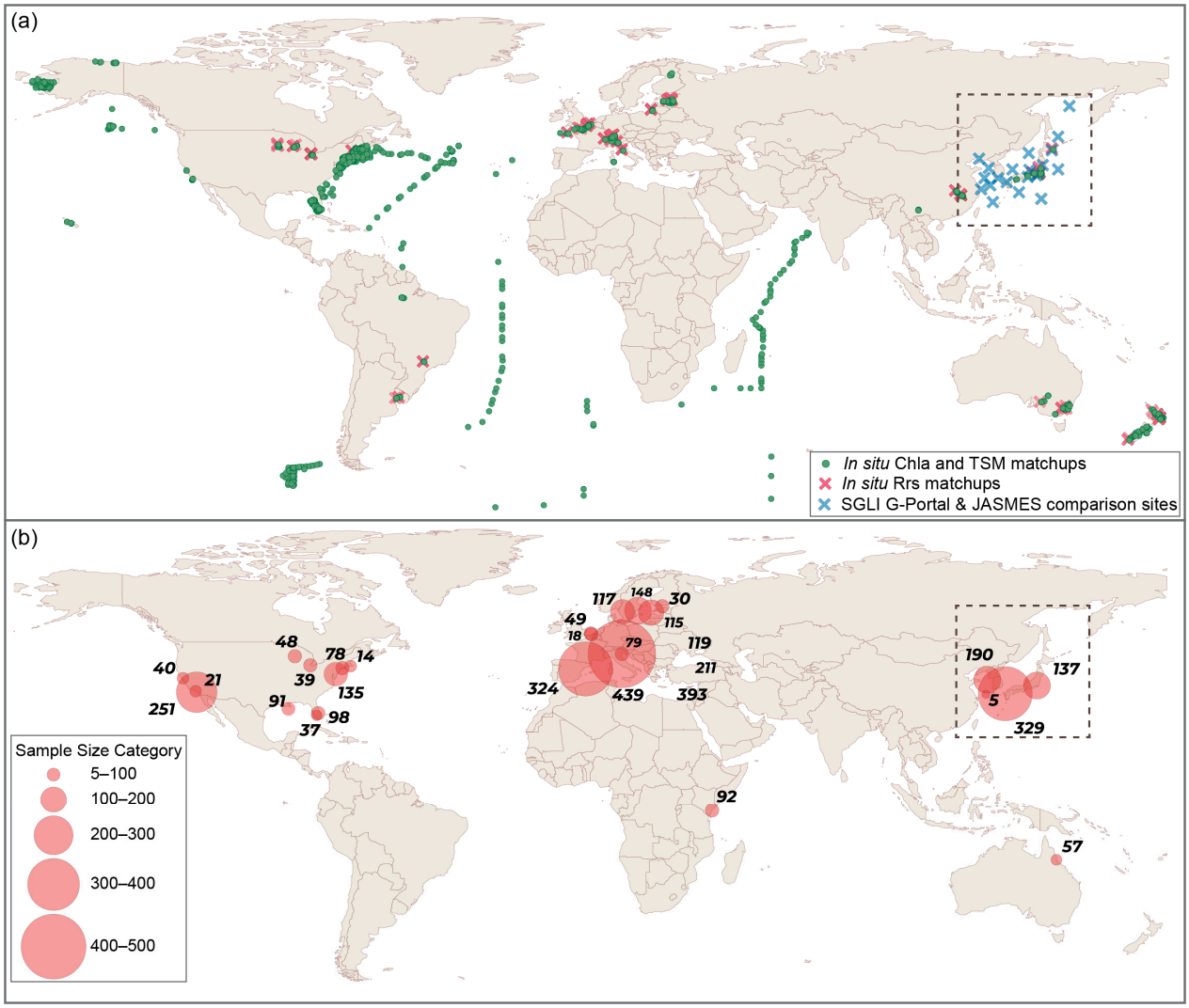

Figure 1. Global distribution of matchups between validation datasets and GCOM-C/SGLI. (**a**) Locations of 331 in situ R_{rs} matchups (red cross), 753 in situ Chla and TSM matchups (green circle) of cruise measurements, and 22 sites for G-Portal and JASMES comparison (blue cross). (**b**) Distribution of 3704 AERONET-OC matchups, with red circles indicating locations and sizes proportional to the number of measurements at each site. The dashed box represents the footprint of the JASMES full-resolution R_{rs} product over Japan.

2.3. G-Portal and JASMES Atmospheric Correction

The atmospheric correction applied for SGLI Level-1B data to derive R_{rs} products differs between G-Portal and JASMES. The G-Portal atmospheric correction, developed by Toratani et al. [28], is JAXA's standard product and is currently in Version 3.0. JASMES atmospheric correction was developed by Hiroshi Murakami [29]. The atmospheric schemes of G-Portal and JASMES are briefly summarized in the following sections.

2.3.1. G-Portal Atmospheric Correction

The atmospheric correction process of G-Portal (Figure 2a) starts with the same system vicarious calibration using in situ R_{rs} data from MOBY and BOUSSOLE datasets to ensure inter-band calibration accuracy [28]. This is followed by a correction for the attenuation of solar radiation due to ozone absorption, utilizing ozone transmittance values based on the solar zenith angle and ozone optical thickness. Next, the process addresses Rayleigh scattering by gas molecules, using pre-calculated Rayleigh reflectance values that depend on the optical thickness of gas molecules and geometric parameters. In cases where the Rayleigh-corrected reflectance of a pixel exceeds 0.07, the atmospheric correction process is skipped. This high-reflectance test helps identify and exclude pixels with high reflectance, such as those from clouds, from further correction, ensuring that atmospheric correction is not applied to highly reflective surfaces.

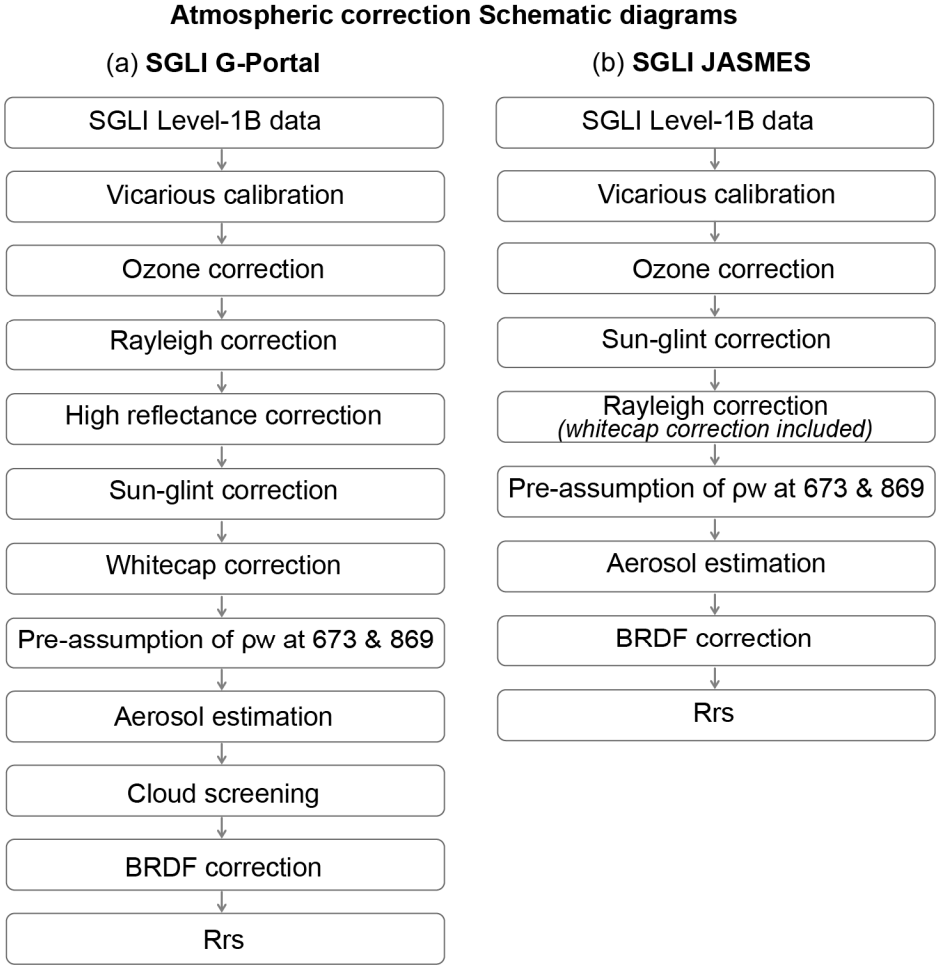

Figure 2. Schematic diagram of atmospheric correction processes for (**a**) SGLI G-Portal and (**b**) SGLI JASMES.

Sun-glint, caused by the direct reflection of sunlight off the water surface, is corrected using the empirical model by Cox and Munk [38], which incorporates wind speed data. Whitecap reflectance, due to foam on the ocean surface, is corrected using wavelength-dependent coefficients and wind speed data.

The initial guess for ρw is intricately related to the Linear Combination Index (LCI) method [39]. The calculation begins by using LCI values (LCI_low and LCI_high) to determine ρw in the near-infrared bands (673 nm and 869 nm). These values are derived from the Rayleigh-corrected reflectance in the 490, 565, and 865 nm bands. For each band, ρw is computed differently based on the ranges of LCI using a fourth-order polynomial determined empirically from data sources like AERONET-OC.

Cloud screening is performed by masking pixels identified as clouds based on an aerosol reflectance threshold of 0.04 or more, ensuring that cloudy pixels do not interfere with the atmospheric correction process. Finally, bidirectional reflectance distribution function (BRDF) correction is applied to adjust for the angular dependence of reflectance [40].

2.3.2. JASMES Atmospheric Correction

The atmospheric correction process of JASMES (Figure 2b) begins with the same system vicarious calibration using in situ R_{rs} data from the MOBY and BOUSSOLE datasets to ensure inter-band calibration accuracy, followed by the same ozone correction using solar zenith angle and ozone optical thickness. Sun-glint reflectance is corrected using the Cox and Munk [38] model, as in G-Portal, and Rayleigh scattering is corrected using pre-calculated reflectance values. Unlike G-Portal, the correction for whitecap reflectance is included in the Rayleigh scattering correction due to the similarity in their spectral shapes.

The aerosol estimation process in JASMES closely mirrors that of G-Portal, encompassing the initial guess of ρw, calculation of LCI, refinement of ρw at near-infrared bands, followed by aerosol optical thicknesses (AOT) and aerosol model selection. The key difference is that in JASMES, the aerosol model is reselected if the ρw at the 412 nm band, rather than the 380 nm band, is negative. BRDF corrections are then applied to account for varying observation and illumination geometries.

2.4. Water Quality Products

This study also investigates the accuracy and agreement of Chla and TSM from both G-Portal and JASMES platforms. Both G-Portal standard products and JASMES NRT products utilize the same algorithms for water quality, with detailed methodologies available at https://suzaku.eorc.jaxa.jp/GCOM_C/data/product_std.html, accessed on 10 December 2024. Similar to NASA's standard Chla approach [41], the JAXA Chla Version-2 algorithm [29] merges the color index (CI) algorithm [42] for low Chla concentrations and the ocean color (OCx) algorithms [43] for high Chla concentrations, as follows:

$$
\begin{aligned}
Chla &= w_{ci} * Chla_{ci} + (1 - w_{ci}) * Chla_{OCx} \\
Chla_{ci} &= 10^{-0.38817+236.59825\times CI} \\
Chla_{OCx} &= 10^{0.39747-3.42876\ x+5.33109x^2-5.399667x^3+1.73379x^4} \\
x &= log_{10}(\max(\tfrac{Rrs(\lambda_3)}{Rrs(\lambda_6)}, \tfrac{Rrs(\lambda_4)}{Rrs(\lambda_6)}, \tfrac{Rrs(\lambda_5)}{Rrs(\lambda_6)}) \\
CI &= R_{rs}(\lambda_6) - \tfrac{R_{rs}(\lambda_3)\times[\lambda_7-\lambda_6]+R_{rs}(\lambda_7)\times[\lambda_6-\lambda_3]}{[\lambda_7-\lambda_3]} \\
w_{ci} &= \tfrac{0.0002+CI}{0.0002-0.0006} \\
&\begin{cases} w_{ci} = 0 & (w_{ci} < 0) \\ w_{ci} = w_{ci} & (0 \le w_{ci} \le 1) \\ w_{ci} = 1 & (w_{ci} > 1) \end{cases}
\end{aligned}
\tag{1}
$$

where λ_3, λ_4, λ_5, λ_6, and λ_7 refer to wavelengths at 443, 490, 530, 565, and 670 nm, respectively. The coefficients for these Chla algorithms were developed using in situ bio-optical data from NASA's bio-Optical Marine Algorithm Dataset (NOMAD) [44] and additional in situ measurements around Japan. The TSM algorithm Version-2, developed by Mitsuhiro Toratani [45], uses the following equation:

$$TSM = 10^{-1.5831\ log_{10}(\frac{Rrs(\lambda_4)}{Rrs(\lambda_6)})+0.3626\ log_{10}(R_{rs}(\lambda_6))+1.2096} \quad (2)$$

where λ_4 and λ_6 refer to wavelengths at 490 and 565 nm, respectively.

2.5. AERONET-OC R_{rs} Dataset

AERONET-OC is a globally distributed network of CE-318 sun-photometers manufactured by CIMEL Electronique (Paris, France) that measure sun, sky, and water surface radiances, providing critical data for calibrating and validating satellite ocean color sensors. The AERONET-OC network was established by NASA and is operated in collaboration with international partners. AERONET-OC sites are mainly located in coastal regions and measure spectral aerosol optical depth, sky radiance, and water-leaving radiance, which are essential for correcting atmospheric effects on satellite data and deriving accurate ocean color products. The processing algorithm is currently Version 3.0 with three data quality levels: Level 1.0 (unscreened), Level 1.5 (cloud-screened and quality-controlled), and Level 2.0 (quality-assured).

AERONET-OC measures the radiance emanating from the water surface (from which normalized water-leaving radiance, nL_W, is expressed in $\mu W/cm^2/nm/sr$) using sun-photometer sensors. AERONET-OC data also feature nL_W values corrected for bidirectional effects, utilizing methodologies from Morel et al. ($L_{Wn-f/Q}$, [46]) and Lee et al. (L_{Wn-IOP}, [47]). Gleason et al. [48] found that Lee's based model outperformed Morel's model in Case 2 waters at small azimuth angles and for Chla greater than the 10 mg/m^3, while Morel's performed better in Case 1 waters. For our analysis, we employed the $L_{Wn-f/Q}$ data. The R_{rs} products were derived using the following formula:

$$R_{rs}(\lambda) = \frac{nL_{W-f/Q}(\lambda)}{F_0(\lambda)} \quad (3)$$

where λ represents the nominal bands of AERONET-OC sun-photometers (Table 1). Comparing the seven SGLI bands in the UV–visible range (Section 2.1) with AERONET-OC bands (Table 1), it is noted that the SGLI 380 nm band does not have a close counterpart band in AERONET-OC. However, for the other six SGLI bands, AERONET-OC sensors have three identical bands (412, 443, and 490 nm) and three very close bands (SGLI: 530, 565, and 670 nm; AERONET-OC: 532, 560, and 667 nm). Although there are several techniques for band-shifting [49,50], we decided to use the nearby bands when comparing SGLI with AERONET-OC to eliminate any uncertainty associated with band-shifting techniques, mainly since the spectral differences are within 5 nm.

Figure 1b illustrates the location of 29 AERONET-OC sites, out of which 5 sites, named Galata_Platform, Gloria, Grizzly_Bay, Palgrunden, and Lucinda, have two sun-photometer configurations that changed during the analysis period (January 2018 and December 2023) as highlighted in Table 1. We downloaded 70,956 Level-2 (quality-assured) records from 29 AERONET-OC sites across the analysis period.

Table 1. Nominal bands of AERONET-OC sun-photometers available between January 2018 and December 2023. Five of the twenty-nine AERONET-OC sun-photometers, denoted with (a) to (e), have old and new sensor configurations. Different colors highlight sensors with the same nominal bands.

AERONET-OC Site	400	412	443	490	510	532	551	555	560	620	667	681	709	779	865	870	1020
AAOT	O	O	O	O	O				O	O	O			O	O		O
Ariake_Tower (†)	O	O	O	O	O				O	O	O			O	O		O
Casablanca_Platform	O	O	O	O	O				O	O	O			O	O		O
Chesapeake_Bay	O	O	O	O	O				O	O	O			O	O		O
Galata_Platform (a)	O	O	O	O	O				O	O	O			O	O		O
Gloria (b)	O	O	O	O	O				O	O	O			O	O		O
Grizzly_Bay (c)	O	O	O	O	O				O	O	O			O	O		O
Gustav_Dalen_Tower	O	O	O	O	O				O	O	O			O	O		O
Helsinki_Lighthouse	O	O	O	O	O				O	O	O			O	O		O
Irbe_Lighthouse	O	O	O	O	O				O	O	O			O	O		O
Kemigawa_Offshore (†)	O	O	O	O	O				O	O	O			O	O		O
Palgrunden (d)	O	O	O	O	O				O	O	O			O	O		O
San_Marco_Platform	O	O	O	O	O				O	O	O			O	O		O
Section-7_Platform	O	O	O	O	O				O	O	O			O	O		O
Galata_Platform (a)		O	O	O		O	O				O					O	O
Gloria (b)		O	O	O		O	O				O					O	O
Ieodo_Station (†)		O	O	O		O	O				O					O	O
LISCO		O	O	O		O	O				O					O	O
Lucinda (e)		O	O	O		O	O				O					O	O
MVCO		O	O	O		O	O				O					O	O
Socheongcho (†)		O	O	O		O	O				O					O	O
Thornton_C-power		O	O	O		O	O				O					O	O
USC_SEAPRISM		O	O	O		O	O				O					O	O
USC_SEAPRISM_2		O	O	O		O	O				O					O	O
Venise		O	O	O		O	O				O					O	O
WaveCIS_Site_CSI_6		O	O	O		O	O				O					O	O
Zeebrugge-MOW1		O	O	O		O	O				O					O	O
Grizzly_Bay (c)		O	O	O	O				O	O	O	O	O		O		O
Lake_Erie		O	O	O	O				O	O	O	O	O		O		O
Lake_Okeechobee		O	O	O	O				O	O	O	O	O		O		O
Lake_Okeechobee_N		O	O	O	O				O	O	O	O	O		O		O
South_Greenbay		O	O	O	O				O	O	O	O	O		O		O
Lucinda (e)		O	O	O				O			O						
Palgrunden (d)		O	O	O				O			O						

(†) AERONET-OC sites under the coverage of both G-Portal and JASMES. (a) Galata_Platform site has two sensor configurations: old (green) and new (blue, from 5 November 2018). (b) Gloria site has two sensor configurations: old (green) and new (blue, from 16 March 2018). (c) Grizzly_Bay site has two sensor configurations: old (green) and new (blue, from 25 May 2019). (d) Palgrunden site has two sensor configurations: old (orange) and new (blue, from 21 June 2019). (e) Lucinda site has two sensor configurations: old (orange) and new (green, from 16 September 2018).

2.6. Field Measurements Dataset

We utilized hyperspectral measurements from the GLObal Reflectance community dataset for Imaging and optical sensing of Aquatic environments (GLORIA, https://doi.org/10.1594/PANGAEA.948492). GLORIA includes 7572 in situ hyperspectral R_{rs} spectra, each linked with one or more biogeochemical measurements such as Chla, TSM, turbidity, absorption of CDOM at 440 nm (aCDOM440), and Secchi depth [51,52]. The dataset spans three decades, covering more than 450 aquatic sites in 25 countries, ranging from lakes and rivers to coastal waters and estuaries. Radiometric measurements were taken using hyperspectral instruments like TriOS-RAMSES, HyperOCR (Sea-Bird Scientific), and multispectral instruments such as C-OPS (Biospherical). Hyperspectral data were interpolated at 1 nm intervals from 350 to 900 nm. Chla was mostly analyzed using solvent-based pigment extraction, predominantly employing 90% acetone, followed by fluorometric and spectrophotometric analyses [51]. Uncorrected Chla values were used when phaeopigment-corrected measurements were unavailable. TSM was measured by weighing the dried residue of pre-weighed filter pads. aCDOM4440 was quantified using spectrophotometry following established protocols like that of Mitchell et al. [53]. Quality control involved procedural checks for spectral anomalies, such as high-frequency variability and baseline shifts. Flags indicated the presence of issues (e.g., 'Noisy_red', 'Baseline_shift'), which were visually inspected and flagged accordingly [51].

In addition to the GLORIA dataset, our field measurements included six waterbodies in Japan: Lake Kasumigaura, Lake Biwa, the Seto Inland Sea, Tokyo Bay, Ariake Bay, and Ise-Mikawa Bay. Radiometric data collection utilized two distinct instruments: (a) three TriOS-RAMSES instruments operating across a spectral range of 350–900 nm; = and (b) a Fieldspec HandHeld-2 Spectroradiometer, covering 350 to 1075 nm. Radiometric measurements for both instruments were conducted from

above water. For the RAMSES instruments, typical measurements involved an irradiance sensor oriented vertically upward to collect downwelling irradiance, while two radiance sensors were positioned approximately 45° from zenith and nadir angles to measure sky radiance and total water-leaving radiance, respectively, as illustrated in the schematic by Lehmann et al. [51]. Measurements using the HandHeld-2 spectroradiometer followed the protocol described by Curtis Mobley [54].

Water samples were collected from the surface layer (0–2 m) for analysis. Chla concentration was measured fluorometrically by filtering water samples through pre-combusted glass fiber filters, followed by pigment extraction using methanol [55]. TSM concentrations were determined by filtering the water samples through pre-weighed filters (e.g., GF/F filters) to retain particulate matter, which was then dried at 105 °C, cooled, and re-weighed, following the standard protocol of [56].

We did not apply BRDF corrections to in situ R_{rs} data due to the isotropic nature of upwelling radiance for small angles that minimizes the angular dependence in R_{rs} estimation [57].

Hyperspectral R_{rs} spectra were resampled at the SGLI bands considering their relative spectral response (RSR) function, as described by the following equation:

$$R_{rs}^{SGLI}(\lambda_j) = \frac{\sum_\lambda R_{rs}^{hyper}(\lambda) \times RSR(\lambda)}{\sum_\lambda RSR(\lambda)} \quad (4)$$

where $R_{rs}^{SGLI}(\lambda)$ is the resampled R_{rs} at the SGLI nominal band λj. $R_{rs}^{hyper}(\lambda)$ and RSR(λ) are the hyperspectral R_{rs} and the corresponding RSR of nominal band λj, respectively.

The dataset was divided into two groups based on their sources to utilize their distinct characteristics. AERONET-OC provides long-term, quality-assured R_{rs} measurements from coastal and offshore locations, enabling robust temporal analysis of satellite performance. In contrast, field campaign datasets encompass diverse inland, coastal, and offshore environments, incorporating additional water quality parameters (e.g., Chla) that facilitate evaluation across trophic gradients. This segmentation assesses satellite performance across varied aquatic environments while maintaining statistical robustness.

2.7. SGLI Matchups

Matchups refer to finding SGLI measurements collected within a short time frame with AERONET-OC and cruise measurements. To facilitate this, we developed SGLICollect (https://github.com/RS-ML-Hub/SGLICollect, accessed on 10 December 2024), an open-source Python-based tool designed to search, download, and extract SGLI data from both G-Portal and JASMES (https://doi.org/10.5281/zenodo.10565662). The search function allows users to locate SGLI products based on geographic coordinates (latitude, longitude) and dates. The download function identifies and retrieves Level-2 SGLI products with a spatial resolution of 250 m that fall within a time window that does not exceed ±5 h from the satellite overpass time. The SGLI/GCOM-C satellite typically captures data at approximately 10:30 AM local solar time, while field measurements are conducted between 8:30 AM and 3:30 PM, resulting in a maximum time difference of ±5 h. It extracts data from a single pixel that matches the search criteria [58], ensuring the satellite measurement directly corresponds to the location of the in situ data and avoids including irrelevant data from adjacent pixels in dynamic and spatially heterogeneous aquatic environments. If multiple satellite images meet the search criteria within the specified time frame, SGLICollect selects the image that provides the maximum coverage over the target pixel. The selected SGLI image is then downloaded, and the data, including R_{rs} at various bands, Chla, TSM, and other products, are extracted.

Using SGLICollect, we identified 3704 matchups from 70,956 AERONET-OC samples measured on the same day. Figure 1b illustrates the spatial distribution of matchups at each AERONET-OC site, while Figure 3a shows the R_{rs} spectra of AERONET-OC compared with SGLI R_{rs} from G-Portal (Figure 3b) and JASMES (Figure 3c). Similarly, the extraction process of SGLICollect with the cruise dataset resulted in 331 matchups. Despite their limited numbers, the matchups of field measurements provide global coverage (Figure 1a) and exhibit higher R_{rs} magnitudes, up to 0.12 1/sr (Figure 3d), compared with SGLI R_{rs} from both G-Portal (Figure 3e) and JASMES (Figure 3f).

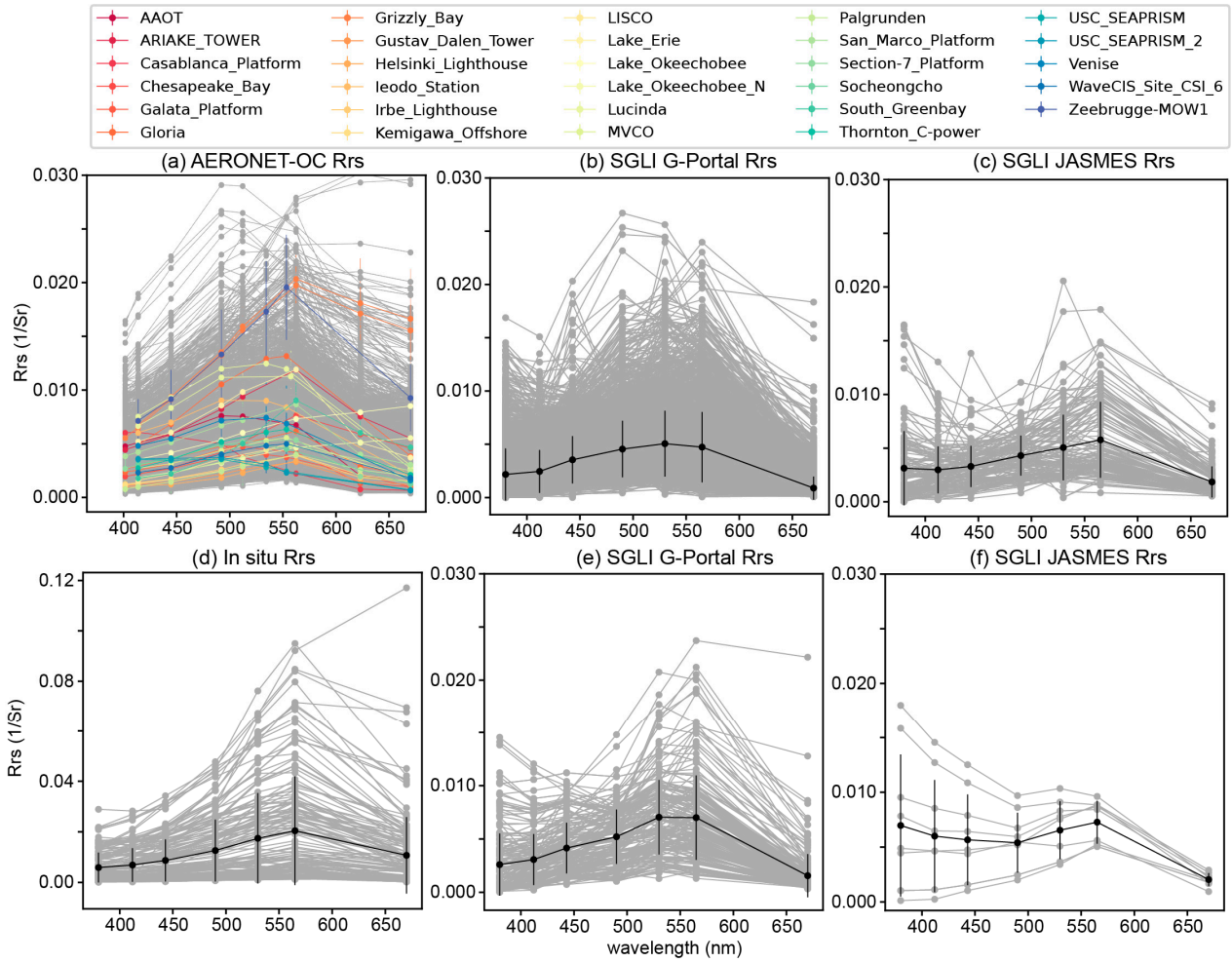

Figure 3. Comparison of R_{rs} spectra for various matchup scenarios. The first row represents R_{rs} spectra for matchups between (**a**) AERONET-OC and both (**b**) SGLI G-Portal and (**c**) SGLI JASMES. The second row shows R_{rs} spectra for matchups between (**d**) cruise measurements and both (**e**) SGLI G-Portal and (**f**) SGLI JASMES. Grey lines represent individual matchups, with black lines indicating the mean R_{rs} values across different wavelengths. The legend at the top identifies the mean R_{rs} values at various AERONET-OC sites, as shown in panel (**a**).

2.8. Evaluation Metrics

The performance of SGLI R_{rs} products was evaluated using various statistical metrics, including bias (β), mean absolute difference (MAD, δ), root mean square difference (RMSD, Δ), and mean absolute percentage difference (MAPD, σ). These metrics are defined as follows:

$$Bias = 10^{z}, \quad where \quad z = \frac{\sum_{i=1}^{N} (log_{10}(E_i) - log_{10}(R_i))}{N} \tag{5}$$

$$MAD = 10^{z}, \quad where \quad z = \frac{\sum_{i=1}^{N} \left| log_{10}(E_i) - log_{10}(R_i) \right|}{N} \tag{6}$$

$$\text{RMSD} = \sqrt{\frac{\sum_{i=1}^{N} (log_{10}(E_i) - log_{10}(R_i))^2}{N}} \tag{7}$$

$$MAPD = \frac{100}{N} * \sum_{i=1}^{N} \frac{| E_i - R_i |}{R_i} \quad (\%) \tag{8}$$

where R_i and E_i refer to reference and evaluated data at sample i. N represents the number of samples. The Theil–Sen slope (S) [59,60] is calculated using "scipy.stats.mstats.theilslopes", where the slopes between all data pairs are computed and the median of these slopes represents the Theil–Sen slope. This method is robust against non-normal data distributions and outliers [61].

The coefficient of determination (R^2) is computed using Type-2 regression [62], which is suitable for real situations where uncertainties are present in both the reference and evaluated datasets [63,64]. Type-2 regression minimizes the perpendicular distance between the data points and the regression line.

The trend and seasonality components were extracted using the "seasonal_decompose" function from the "statsmodels" Python library. This function applies an additive decomposition to time series data, assuming that the observed values can be represented as the sum of the trend, seasonality, and residual components [65]. The decomposition was performed after resampling the data to a weekly scale and interpolating to handle missing values.

The Pearson correlation coefficient was calculated using the "pearsonr" function from the "scipy.stats" library to measure the linear correlation between the trend and seasonality components across datasets (G-Portal, JASMES, and AERONET-OC).

3. Results

3.1. Assessment of R_{rs} Products Using AERONET-OC

The evaluation of SGLI R_{rs} products from G-Portal and JASMES was first conducted using AERONET-OC matchups over six years of the GCOM-C/SGLI mission (January 2018–December 2023). Since JASMES full-resolution (250 m) R_{rs} products are available only around Japan (Section 2.2 and dashed box in Figure 1a), the comparison between AERONET-OC R_{rs} and SGLI R_{rs} from G-Portal and JASMES was performed at four AERONET-OC sites: Ieodo_Station, Socheongcho, Ariake_Tower, and Kemigawa_Offshore. Scatterplots in Figure 4. indicate a systematic underestimation of R_{rs} by JASMES across all bands, with a significant underestimation trend at 412 nm, where data points concentrate near zero. Both G-Portal and JASMES show the lowest accuracy at the 412 nm band, with MAPD values of 71.3% and 107.2%, respectively.

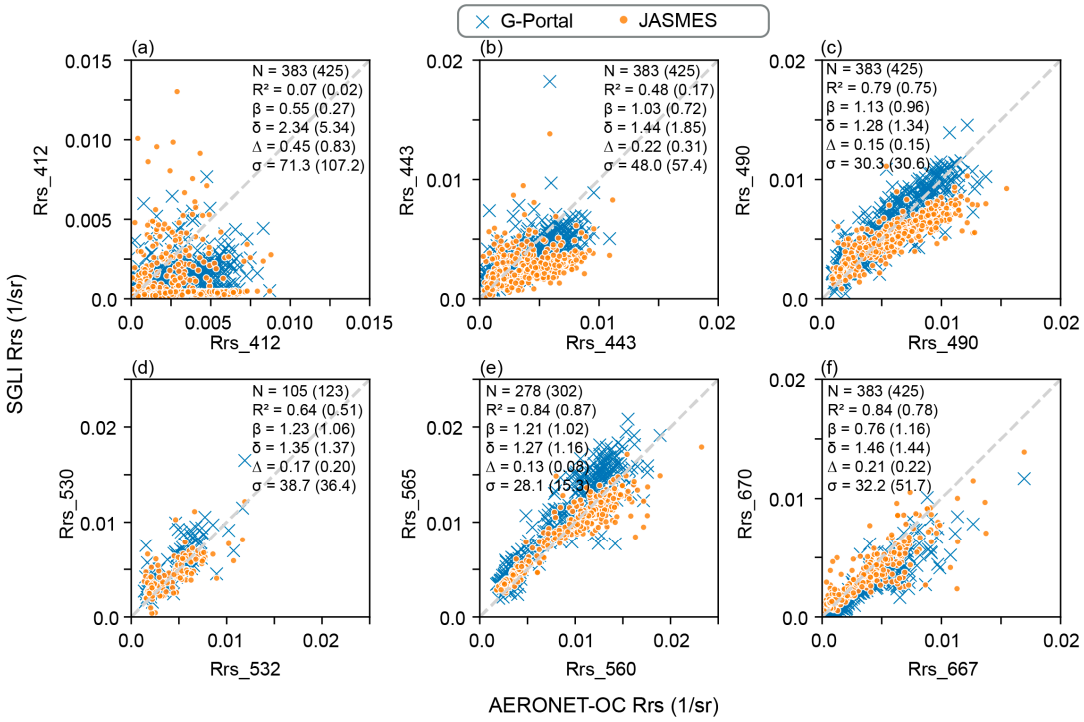

Figure 4. Scatterplots (**a**–**f**) comparing AERONET-OC R_{rs} with SGLI R_{rs} of G-Portal (x symbols) and JASMES (• symbols) over Japan at four AERONET-OC sites: Ieodo_Station, Socheongcho, Ariake_Tower, and Kemigawa_Offshore. N refers to the number of matchups, R^2 to the coefficient of determination, β to bias, δ to mean absolute difference, Δ to root mean square difference, and σ to mean absolute percentage difference in percent (%). For each wavelength, the evaluation metrics for G-Portal are listed first, followed by those for JASMES in parentheses. The dashed grey line represents the 1:1 line.

G-Portal outperforms JASMES in the blue bands (particularly at 412, and 443 nm), demonstrating higher correlation and lower errors. In the green–red bands (532, 565, and 667 nm), G-Portal and JASMES have comparable performance, with JASMES showing slightly better metrics (R^2, bias, MAD, RMSD, and MAPD) at 565 nm (Figure 4e). JASMES generates more matchup data than G-Portal (highlighted as N, Figure 4), with an increase of approximately 12% at all bands.

The evaluation of G-Portal at 29 AERONET-OC global sites (Figure 5) provides similar characteristics to those drawn from the Japan and East Asia evaluation in Figure 4. The 412 nm band shows the poorest performance, with the lowest R^2 of 0.36 and highest MAD, RMSD, and MAPD of 1.91, 0.37, and 58.5%, respectively. The accuracy of SGLI G-Portal R_{rs} improves with increasing wavelength, where the 565 nm band exhibits the best overall performance with the highest R^2 of 0.88. Also, RMSD and MAPD at the 565 nm band performed better by 2.6-fold and 64.86% compared with the 412 nm band. The 667 nm band shows a decline in performance compared to the green bands, with an R^2 of 0.70, as shown in Figure 5f.

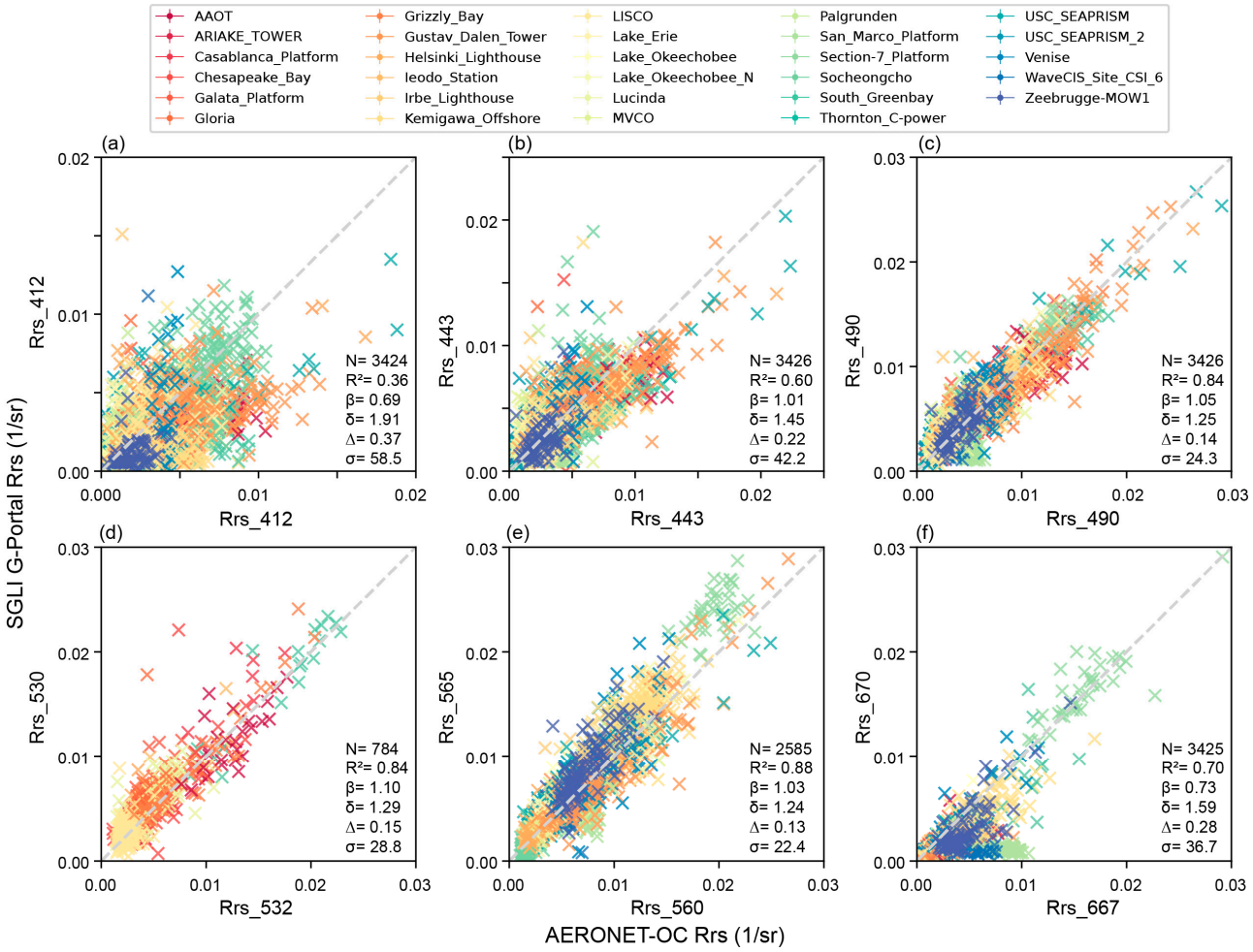

Figure 5. Scatterplots (**a**–**f**) comparing AERONET-OC R_{rs} values with SGLI G-Portal R_{rs} values at 29 AERONET-OC sites, covering z global scale. N refers to the number of matchups, R^2 to the coefficient of determination, β to bias, δ to mean absolute difference, Δ to root mean square difference, and σ to mean absolute percentage difference in percent (%). The dashed grey line represents the 1:1 line.

Figure 6 presents time series plots of R_{rs} values at SGLI bands for three AERONET-OC sites: Kemigawa_Offshore, Ariake_Tower, and Socheongcho. The discrepancies between AERONET-OC and both G-Portal and JASMES are more pronounced at shorter wavelengths (412 nm and 443 nm) across the three sites. SGLI G-Portal aligns with AERONET-OC data better than JASMES at these shorter wavelengths. Both G-Portal and JASMES show improved agreement with AERONET-OC data at longer wavelengths (530 nm, 565 nm, and 670 nm), exhibiting tighter clustering around

the AERONET-OC values. The tendency of JASMES to underestimate R_{rs} values is prominent, particularly at the 412 band. The systematic underestimation of R_{rs} values by JASMES diminishes at longer wavelengths, showing better alignment up to the 565 nm band. However, this changes to an overestimation trend at 670 nm, particularly at the Kemigawa_Offshore and Socheongcho sites (Figure 6).

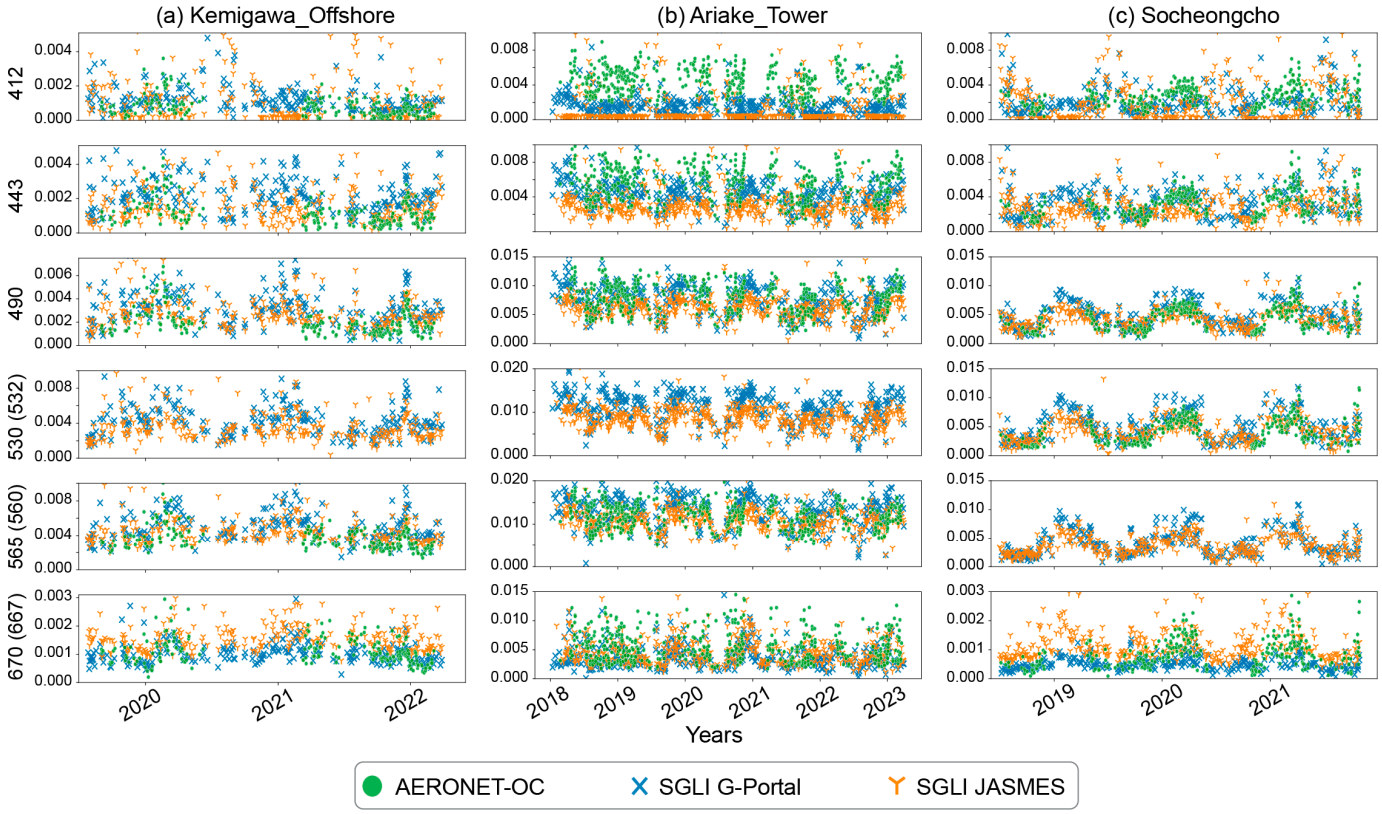

Figure 6. Time series plots comparing R_{rs} values from AERONET-OC (green circles), SGLI G-Portal (blue crosses), and SGLI JASMES (orange fork) across three observation sites: Kemigawa_Offshore, Ariake_Tower, and Socheongcho. Each row corresponds to specific SGLI bands (412 nm, 443 nm, 490 nm, 530 nm, 565 nm, and 670 nm). Parenthetical numbers adjacent to each SGLI band on the Y-axes indicate the closest corresponding AERONET-OC band. For instance, 670 (667) on the *Y*-axis of the last row represents the SGLI and AERONET-OC bands 670 nm and 667 nm, respectively.

The R_{rs} magnitudes are comparable among the three AERONET-OC sites up to the 490 nm band; however, the Ariake_Tower site shows higher R_{rs} magnitudes than the other two sites, starting from the 530 nm to the 670 nm band. The temporal distribution of data points in Figure 6. also shows that both satellite datasets (G-Portal and JASMES) capture seasonal and interannual variations similarly to AERONET-OC data, particularly from the 490 nm band onward toward the 670 nm band. The temporal patterns do not exhibit significant differences among the three sites, suggesting consistent data acquisition and processing over time.

3.2. *Assessment of R_{rs} Products Using Cruise Measurements*

Evaluating both SGLI satellite R_{rs} products from G-Portal and JASMES using cruise measurements adds new value as these data cover different domains, such as open ocean and inland waters (Figure 1a), exhibiting unique optical characteristics. This is evidenced by the higher R_{rs} magnitudes observed in the cruise data compared to AERONET-OC data, as shown in Figure 3a,d. The number of matchups is quite limited, particularly for JASMES whose full-resolution products are available only over Japan (Section 2.2), resulting in 306 samples for G-Portal and only 13 samples for JASMES, which further drop to 94 and 12, respectively, at 380 nm.

Figure 7 indicates that both G-Portal and JASMES show poor agreement with cruise data at the 380 nm band, with high MAPD values (204% for G-Portal and 380% for JASMES). The 412 nm band also shows low agreement, with MAPD values remaining high (90.3% for G-Portal and 251.4% for JASMES), indicating significant discrepancies between the satellite and cruise measurements. From the 443 nm to 565 nm bands, the agreement between cruise measurements and SGLI R_{rs} products improves at lower R_{rs} magnitudes.

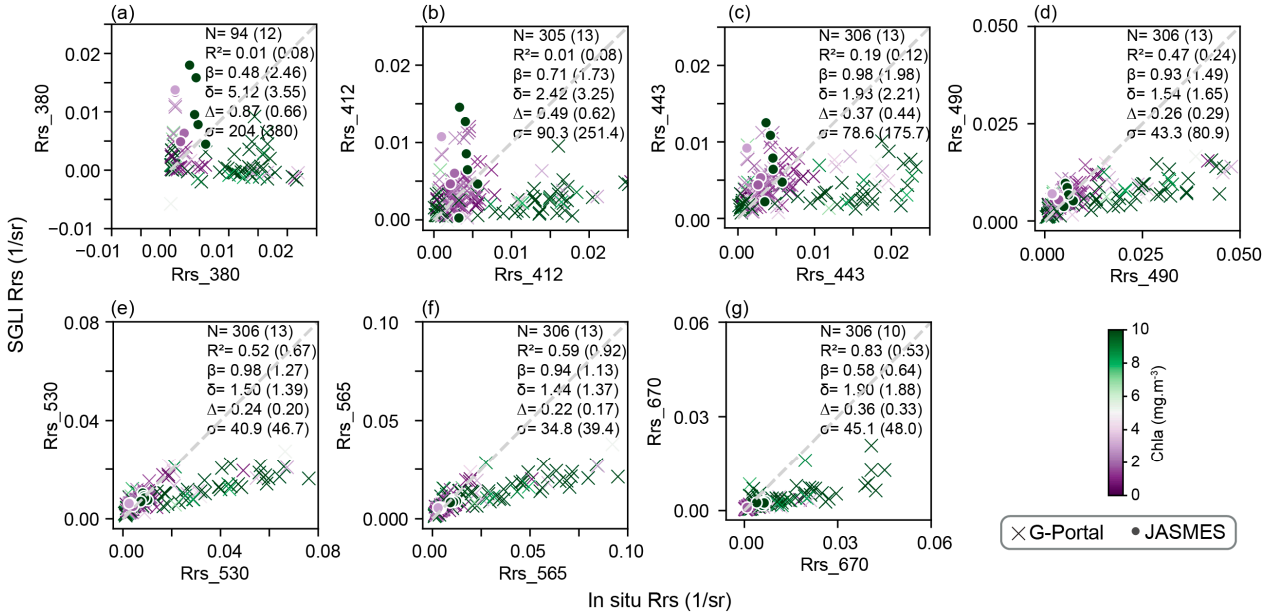

Figure 7. Scatterplots (**a**–**g**) compare cruise R_{rs} with SGLI R_{rs} of G-Portal (x symbols) and JASMES (• symbols). The number of matchups (N), coefficient of determination (R^2), bias (β), mean absolute difference (δ), root mean square difference (Δ), mean absolute percentage difference (σ) in percent (%), and chlorophyll-a (Chla) are shown. For each wavelength, the metrics for G-Portal are listed first, followed by those for JASMES in parentheses. The dashed grey line represents the 1:1 line.

A clear underestimation trend is observed when Chla concentrations exceed 5 mg/m^3, particularly for G-Portal data. This underestimation becomes more apparent at high R_{rs} magnitude; for instance, at the 443 nm band, there is good agreement between cruise measurements and G-Portal for R_{rs} values up to 0.01 1/sr. Beyond this point, the underestimation trend increases for R_{rs} values up to 0.025 1/sr. A similar underestimation trend at the 670 nm band (Figure 7g) is linked with Chla concentrations above 5 mg/m^3. Overall, the agreement between the datasets and cruise measurements improves with increasing wavelength and lower Chla concentrations. G-Portal shows better agreement with cruise measurements compared to JASMES, which is evident from the lower Bias and MAPD across all G-Portal bands compared to JASMES.

The difference in R_{rs} values between SGLI and cruise measurements (ΔR_{rs}), shown in Figure 8. highlights systematic differences in the performance of G-Portal and JASMES compared to cruise data. G-Portal matchups from the global scale consistently show a negative mean ΔR_{rs} across all wavelengths, indicating a general underestimation of R_{rs} values. This underestimation is most pronounced at the 565 nm band, primarily due to the significant underestimation of G-Portal associated with higher R_{rs} magnitudes. G-Portal matchup data over Japan shows ΔR_{rs} values that fluctuate closely around zero. On the other hand, JASMES mean ΔR_{rs} exhibits an overestimation trend that gradually decreases to zero at 530 nm, followed by an underestimation trend at the 565 and 670 nm bands (Figure 8c). G-Portal shows less variability in ΔR_{rs} than JASMES over Japan (Figure 8b,c), particularly at shorter wavelengths. Despite the overall trend of underestimation, the relatively tight clustering around the zero for G-Portal suggests many instances where G-Portal R_{rs} values closely match the AERONET-OC measurements.

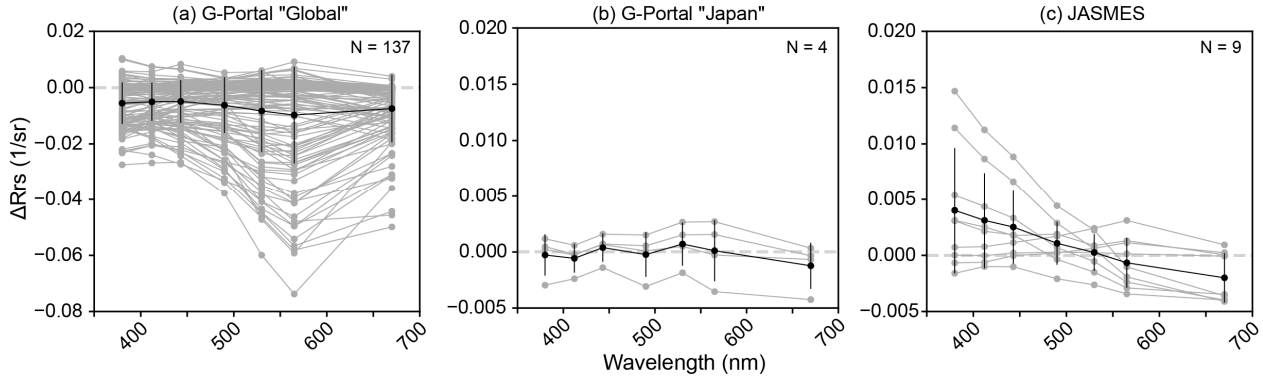

Figure 8. Difference in R_{rs} values (ΔR_{rs}) between cruise measurement and SGLI of (**a**) G-Portal globally, (**b**) G-Portal over Japan, and (**c**) JASMES. N refers to the number of matchups. Each grey line represents individual observations, while the black line indicates the mean ΔR_{rs}, and the vertical bars represent the standard deviation of ΔR_{rs} at each wavelength.

3.3. Performance of SGLI Water Quality Products

Chla and TSM products from the SGLI G-Portal and JASMES were evaluated using in situ measurements, as illustrated in Figure 9. G-Portal generally provides more matchups due to its global coverage, whereas JASMES full-resolution products are limited to Japan. The agreement in terms of R^2 between in situ measurements and the two products is relatively low for both platforms. G-Portal demonstrated lower MAD and RMSD values than JASMES, reflecting a two- to three-fold improvement in Chla and an 18% reduction in the TSM product. Conversely, JASMES performed better in bias and MAPD, with 32–83% improvements for Chla and TSM. G-Portal outperforms JASMES in absolute difference metrics (MAD and RMSD), indicating that G-Portal estimates are closer to the in situ values. Meanwhile, JASMES outperforms G-Portal in bias and MAPD, suggesting that JASMES errors are more consistent and proportional across different concentration levels. Both platforms displayed a tendency to underestimate high concentrations of Chla and TSM.

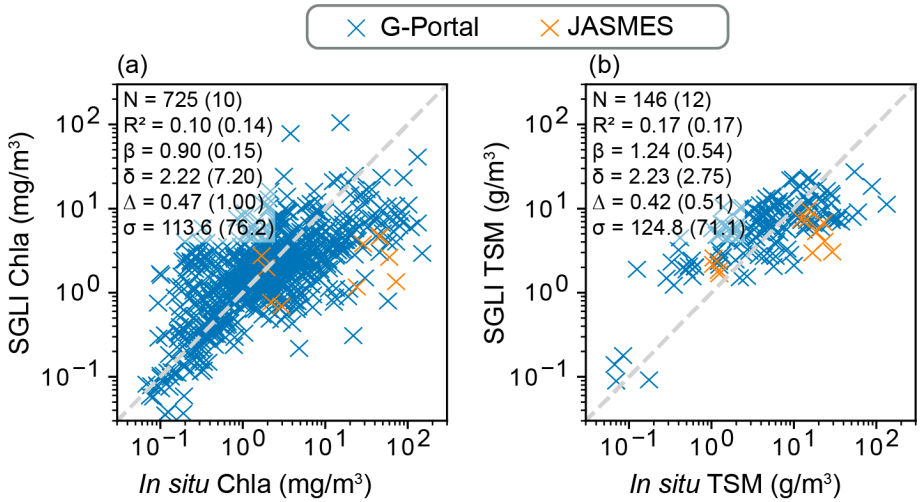

Figure 9. Scatterplots comparing in situ measurements and SGLI-derived values from G-Portal and JASMES for two products: (**a**) Chla and (**b**) TSM. The number of matchups (N), coefficient of determination (R^2), bias (β), mean absolute difference (δ), root mean square difference (Δ), and mean absolute percentage difference (σ) in percent (%) are shown. The metrics for G-Portal are listed first, followed by those for JASMES in parentheses. The dashed grey line represents the 1:1 line.

3.4. Agreement Analysis Between SGLI G-Portal and JASMES Products

The agreement and discrepancies between SGLI JASMES and SGLI G-Portal R_{rs} values were assessed across 22 sites in Japan and East Asia (blue cross, Figure 1a), encompassing both Case 1 and Case 2 waters. The evaluation of R_{rs} products across various SGLI bands indicates that JASMES tends

to provide lower R_{rs} values compared with G-Portal across all bands except at 670 nm, as shown in Figure 10. The 380 nm band has a significantly lower number of matchups (N = 6189), approximately 34% fewer than other bands, primarily due to flagged data points. Specifically, JASMES flagged 3294 samples, while G-Portal flagged 1154 samples, with G-Portal also having 337 samples with negative R_{rs} values. At the 412 nm band, a significant underestimation trend is observed (red dotted oval, Figure 10b), with a high number of values near zero. The agreement between SGLI G-Portal and JASMES improves starting at the 490 nm band and continues to improve with increasing wavelength. The best performance is observed in the green–red bands (530, 565, and 670 nm), with R^2 values ranging from 0.93 to 0.97.

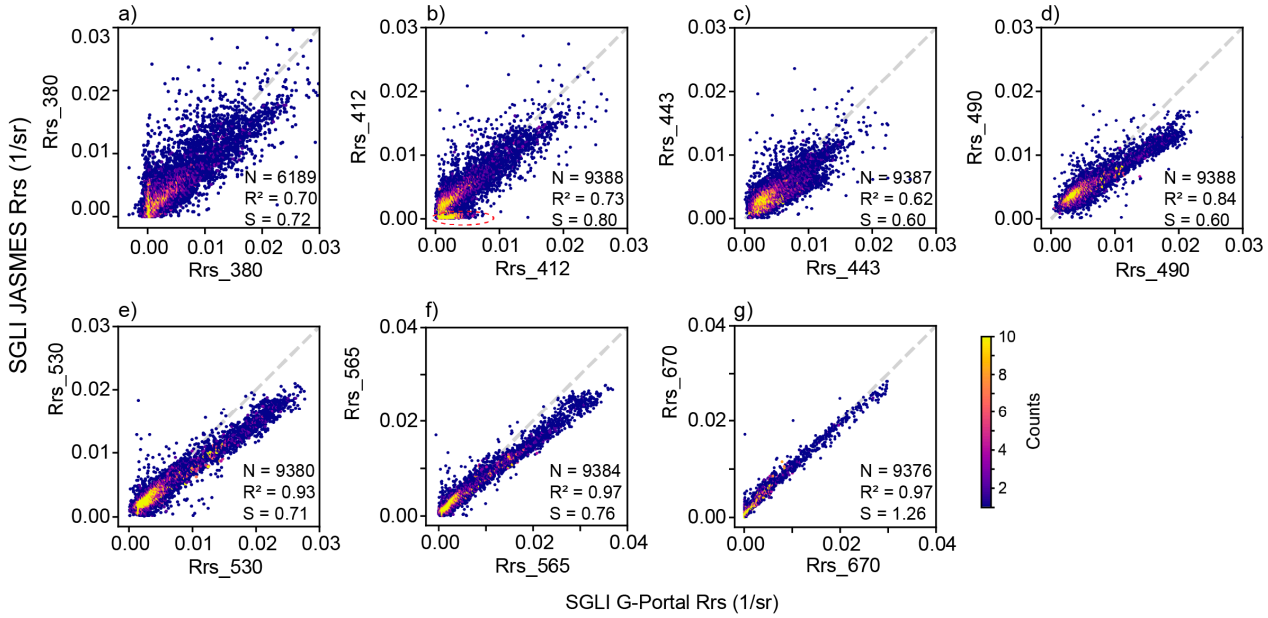

Figure 10. Density scatterplots (**a**–**g**) illustrate SGLI G-Portal R_{rs} versus SGLI JASMES R_{rs} over 22 sites (blue cross, Figure 1a). N refers to the number of matchups, while R^2 and S denote the coefficient of determination and the slope, respectively. The dashed grey line represents the 1:1 line.

The comparison of the SGLI G-Portal and JASMES for Chla and TSM reveals a good agreement for Chla concentrations (Figure 11a) with an R^2 value of 0.45. The TSM measurements (Figure 11b) show a robust correlation with an R^2 of 0.93 and a slope close to unity (0.99), indicating a high level of consistency between the platforms in detecting TSM concentrations.

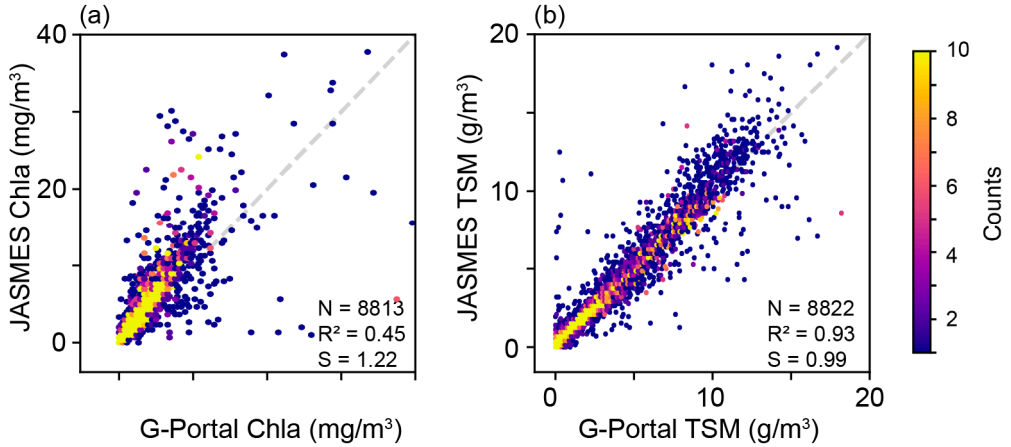

Figure 11. Density scatterplots comparing SGLI G-Portal and SGLI JASMES for (**a**) Chla and (**b**) TSM over 22 sites covering Case 1 and Case 2 waters (blue cross, Figure 1a). N refers to the number of matchups, while R^2 and S denote the coefficient of determination and the slope, respectively. The dashed grey line represents the 1:1 line.

4. Discussion

4.1. Impact of Atmospheric Correction Differences on G-Portal and JASMES

The atmospheric correction processes of G-Portal and JASMES share some similarities, including the use of system vicarious calibration, ozone correction, and the application of the LCI method for aerosol estimation. However, there are notable differences in their processing order and specific corrections applied. In G-Portal, the sun-glint correction is applied after Rayleigh correction, whereas in JASMES, sun-glint correction occurs before Rayleigh correction. Additionally, G-Portal reselection of the aerosol model occurs if the ρw at the 380 nm band is negative, assigning a zero value to ρw. In contrast, JASMES performs this step if the ρw at the 412 nm band is negative. Assigning zero to ρw at the 412 nm band in JASMES could explain the observed concentration of R_{rs} values near zero at this wavelength (Figure 4). Although cruise measurements suggest a tendency for JASMES to overestimate R_{rs} at shorter wavelengths (Figure 7), this observation is potentially skewed by the limited number of cruise samples (only 13), which may not represent broader variability.

The G-Portal atmospheric correction Version 3 [28] introduced several improvements over Version 2.0 [66]. These enhancements included changes in the calculation method of aerosol reflectance using the LCI method, updates to the aerosol look-up table, and improvements in the calculation method of transmittance. Despite these refinements aimed at enhancing the accuracy of aerosol reflectance estimation, particularly in high-turbidity waters, G-Portal still tended to underestimate high R_{rs} magnitudes when evaluated against in situ datasets. The key unresolved issue is the insufficient consideration of inorganic suspended matter in coastal areas within the ocean bio-optical model component of the current atmospheric correction scheme, resulting in significant impacts on R_{rs} values. Toratani et al. [66] reported a similar underestimation trend for nLw that exceeds 0.7 $\mu W/cm^2/nm/sr$ at 670 nm.

Furthermore, the aerosol model used for atmospheric correction in G-Portal employs predefined aerosol types, which may not accurately represent the complex and variable nature of aerosols in coastal regions [66]. This discrepancy can lead to errors in the atmospheric correction process, particularly for higher R_{rs} values. Thus, while Version 3 includes important updates, the fundamental issues identified in Version 2.0 regarding underestimating high R_{rs} values remain relevant.

Notably, JASMES produced approximately 12% more matchup data than G-Portal (as indicated by N in Figure 4). This higher number of matchups may be attributed to differences in data flagging criteria between the two platforms. G-Portal applies stricter thresholds by masking pixels with Rayleigh-corrected reflectance > 0.07 or pixels with aerosol reflectance $\geq$ 0.04, as discussed in Section 2.3.1. These steps ensure that highly reflective surfaces, such as clouds, are excluded from further atmospheric correction. In contrast, JASMES does not implement these high-reflectance-masking steps, likely resulting in more matchups.

4.2. Wavelength-Dependent Accuracy

The performance of the SGLI R_{rs} products from G-Portal and JASMES exhibits considerable variability across different spectral bands. Notably, shorter wavelengths, such as 380 nm and 412 nm, demonstrate less accuracy and higher errors when compared to longer wavelengths like 565 nm and 670 nm. This variability in performance can be attributed to multiple factors influencing measurement accuracy at different spectral bands.

4.2.1. Challenges at Shorter Wavelengths

R_{rs} values at shorter wavelengths show less agreement with AERONET-OC and cruise datasets when compared to their longer wavelength counterparts. This decreased performance can be attributed to several factors, including errors in aerosol model selection and the challenges associated with extrapolating aerosol contributions to shorter bands. Both G-Portal and JASMES use 670 and 869 nm bands to choose aerosol models from predefined sets of aerosol models [28,29]. The extrapolation error of aerosol contribution notably increases with increasing the distance from the near-infrared bands, peaking at UV–blue bands [27]. Furthermore, aerosols in these shorter wavelengths absorb more in the visible spectrum, particularly blue light [67].

Additionally, retrieving accurate R_{rs} in shorter bands is challenging due to the weak water-leaving signal, especially in Case 2 waters, where there is substantial absorption by phytoplankton [68]

and/or CDOM [69]. This absorption significantly diminishes the R_{rs}, given the inverse relationship between absorption and reflectance. Notably, the AERONET-OC and cruise data predominantly originate from coastal zones, typically characterized as Case 2 waters, as shown in Figure 1b. This suggests that the atmospheric correction models used by G-Portal and JASMES may not be suitable for these turbid waters. Researchers have proposed specialized atmospheric correction models for such environments for various ocean color missions [23,70,71], including SGLI [72,73]. Estimating the R_{rs} in the UV region (360–400 nm) from the visible range (410–670 nm), as proposed by Wang et al. [74], can be a potential solution to improve the accuracy of shortwave atmospheric correction.

4.2.2. Improved Accuracy at Longer Wavelengths

The performance significantly improves at longer wavelengths, particularly for the 565 nm band. This improvement can be attributed to a significant reduction in constituents' absorption, where CDOM absorption exponentially decays from the shorter to the longer band, and the phytoplankton absorption also decreases beyond 480 nm and reaches a minimum at around 550 nm [8,75]. Additionally, aerosol properties have a less pronounced effect at longer wavelengths. Furthermore, SGLI exhibits higher signal-to-noise ratios (SNRs) at longer wavelengths, increasing from 509 at the 490 nm band to 1045 at the 560 nm band (Table A1). This improvement in SNR enhances the precision and accuracy of the measurements.

Despite the generally good performance of the 670 nm band, a noticeable decline in accuracy is observed compared to the 565 nm band. This decline may be linked to the strong absorption of phytoplankton at the red region around 675 nm, resulting in a weak R_{rs} signal [75–78]

Overall, the spectral performance and wavelength-dependent accuracy of the SGLI R_{rs} products from G-Portal and JASMES confirm the complexities and challenges inherent in ocean color remote sensing. The inclusion of the unique 380 nm band in SGLI, which is absent in many previous multispectral ocean color sensors, provides additional insights, particularly in retrieving water constituents like aCDOM. While shorter wavelengths are more vulnerable to atmospheric errors, leading to reduced agreement with in situ data, longer wavelengths benefit from diminished atmospheric interference and less pronounced constituent absorption, enhancing accuracy and reliability. Understanding these spectral characteristics is crucial for refining remote sensing algorithms and improving the quality of satellite-derived ocean color data.

4.3. Temporal Consistency and Seasonal Variations in R_{rs} Data

Assessing the temporal consistency and ability of G-Portal and JASMES to capture seasonal and interannual variations in R_{rs} data is crucial for evaluating their reliability in monitoring coastal and oceanic environments. By comparing the temporal patterns observed in the satellite datasets with those from AERONET-OC measurements across multiple years, we can gain insights into the performance of these satellite products.

Temporal consistency measures the ability of a dataset to maintain stable and reliable measurements over time. The time series plot at three AERONET-OC sites (Figure 6) indicated that the G-Portal data generally exhibit a consistent pattern over the years. While there are fluctuations in G-Portal R_{rs} values, they remain relatively stable compared to AERONET-OC measurements, indicating good temporal consistency. While JASMES generally maintains temporal consistency, noticeable trends and variability are observed in specific bands and sites. For instance, an underestimation trend is evident at the 412 nm band, whereas an overestimation trend is seen at the 670 nm band, particularly at the Kemigawa_Offshore site.

Seasonal variations highlight changes in R_{rs} values at different seasons, reflecting natural environmental changes such as phytoplankton blooms, sediment resuspension, and variations in water clarity. Across the three AEONET-OC sites, there appear to be some recurring seasonal patterns in the R_{rs} values (Figure 6). The degree of seasonal variability differs between locations. For example, Ariake Tower shows more pronounced fluctuations than Kemigawa Offshore and Socheongcho, indicating that local factors might influence the extent of seasonal changes.

To further evaluate the coherence of temporal patterns, we performed a quantitative analysis using time series data from the Socheongcho AERONET-OC site as a case study. Trend and seasonality components were extracted for five bands (412, 443, 490, 530, and 670 nm), and correlation coefficients between G-Portal (GP), JASMES (JS), and AERONET-OC (OC) were calculated (Figure A1, Table A2).

The seasonality analysis reveals that G-Portal demonstrates stronger agreement with AERONET-OC than JASMES at shorter wavelengths. For instance, at 412 and 443 nm, the seasonality correlation coefficients for GP–OC are 0.60 and 0.87, respectively, compared to −0.19 and 0.12 for JS–OC. The seasonality correlations for JASMES improve significantly from the 490 nm band onward, with values of 0.93 and 0.88 for GP–OC and JS–OC, respectively. At the red band (670 nm), both GP and JS exhibit moderate seasonality agreement with OC, with GP–OC achieving a correlation of 0.68 and JS–OC 0.46.

The trend correlation analysis shows relatively low agreement between both GP–OC and JS–OC, except at the 443 nm band, where JS–OC achieves a high trend correlation of 0.85 compared to 0.58 for GP–OC. These results corroborate the qualitative observations that G-Portal outperforms JASMES in capturing temporal patterns at shorter wavelengths, while both platforms achieve improved consistency at longer wavelengths.

While the consistent data acquisition and processing over time suggest that both G-Portal and JASMES have the potential to monitor temporal patterns effectively, the analysis of trends reveals some limitations in achieving the high radiometric stability required for long-term monitoring of radiometric variables. For instance, Zibordi and Mélin [79] reported a benchmark of 0.5% per decade radiometric stability for climate data records. Given the current evaluation period (2018–2023), it is likely too early to definitively assess the long-term monitoring capability of SGLI products. Continued assessments and longer time series data are essential to determine the radiometric stability and robustness of these datasets for climate applications.

4.4. Performance Insights on SGLI Chla and TSM

Our analysis of the SGLI-derived water quality products, Chla and TSM, provides insights into the performance of G-Portal and JASMES for these parameters. Both platforms tend to underestimate high Chla and TSM concentrations, as shown in Figure 9. This underestimation can be attributed to the optical complexity in turbid waters, where multiple absorbing and scattering substances interfere with accurate retrieval, affecting algorithm performance for high values.

On the other hand, the observed agreement between G-Portal and JASMES for Chla and TSM may be due to the specific wavelengths used in the algorithms for these products. Both platforms use the same methodologies for Chla and TSM retrieval. For TSM, which primarily relies on the 490 nm and 565 nm bands, we observed better consistency between satellite-derived and in situ measurements, as well as between the two platforms (Section 2.4). Chla retrieval, however, is more variable due to additional bio-optical complexities and reliance on a broader wavelength set. This variability likely explains the lower R^2 values for Chla compared to TSM (Figure 11), reflecting greater sensitivity to environmental conditions and water constituents.

To enhance the long-term applicability of GCOM-C/SGLI data for water quality monitoring, future research should prioritize developing and refining Chla and TSM algorithms. Such advancements would enable more reliable and consistent analyses over extended periods, contributing to improved global water quality monitoring.

5. Conclusions

This study evaluated the R_{rs} products from the GCOM-C/SGLI, provided through JAXA's two platforms, G-Portal and JASMES, using matchups from AERONET-OC and cruise measurements collected between January 2018 and December 2023. The results revealed distinct differences between the two platforms. JASMES provided lower R_{rs} magnitudes than G-Portal across all bands except at 670 nm. JASMES significantly underestimated R_{rs} at the 412 nm band, with values clustering around zero. In contrast, G-Portal performed better at shorter wavelengths, showing lower errors and better correlation. JASMES generates approximately 12% more matchup data than G-Portal, primarily due to G-Portal's stricter data flagging criteria for masking high-reflectance areas. Due to flagged or negative values, there were also significantly fewer matchups, by 3–5-fold, at the 380 nm band than other bands. Additionally, G-Portal tended to underestimate R_{rs} measurements with high Chla concentrations and high R_{rs} magnitude, primarily due to inadequate consideration of inorganic suspended matter and inaccurate representation of predefined aerosol models in coastal areas. These findings underscore the complexities and challenges of atmospheric correction observed in the UV and blue bands (380 and 412 nm), compared to longer wavelengths. The agreement analysis between G-Portal and

JASMES showed improved alignment starting from the 490 nm band, with the highest concordance observed in the green–red bands (530, 565, and 670 nm), where R^2 values were approximately 0.94. The temporal analysis over Japan and East Asia revealed that G-Portal data provide stable and reliable measurements over time, aligning closely with AERONET-OC observations despite minor fluctuations. JASMES, on the other hand, generally maintains temporal consistency but exhibits greater variability, with an underestimation trend at 412 nm and an overestimation trend at 670 nm, particularly at the Kemigawa_Offshore site. The analyses at the Socheongcho site further indicate that while seasonality is well captured, trends are less consistent. The agreement between in situ measurements and the two water quality products (Chla and TSM) was relatively low for both platforms. In summary, while both G-Portal and JASMES have demonstrated capabilities in capturing spatial and temporal variations in ocean color, there are areas for improvement, particularly in the atmospheric correction of shorter wavelengths and over Case 2 waters. Addressing these challenges will be essential for advancing the utility of SGLI R_{rs} products in ocean monitoring and related climate research.

Author Contributions: Conceptualization, S.I.S. and H.H.; methodology, S.I.S., M.T., H.H. and S.S.; software, S.I.S.; validation, S.I.S.; formal analysis, S.I.S.; investigation, S.I.S.; resources, S.I.S.; data curation, S.I.S., H.H. and J.I.; writing—original draft preparation, S.I.S.; writing—review and editing, S.I.S., H.H., S.S. and E.S.; visualization, S.I.S.; funding acquisition, S.I.S., H.H., S.S. and E.S. All authors have read and agreed to the published version of the manuscript.

Funding: This research was supported by the Kyoto University of Advanced Science (KUAS) Advanced Research Grant, the Japan Aerospace Exploration Agency (JAXA) under the Global Change Observation Mission for Climate (GCOM-C) RA7 grant, the Asia-Pacific Network for Global Change Research (APN) project number CRRP2024-05MY-Siswanto and NOAA grant NA24NESX4320001 (Cooperative Institute for Satellite Earth System Studies–CISESS) at the University of Maryland/ESSIC.

Data Availability Statement: Satellite data is accessible through the G-Portal and JASMES portals. GLORIA and AERONET-OC data are publicly available as described in the manuscript.

Acknowledgments: The scientific results and conclusions, as well as any views or opinions expressed herein, are those of the authors and do not necessarily reflect those of NOAA or the US Department of Commerce. The authors would like to thank the reviewers for their valuable feedback, which has significantly enhanced the quality of the manuscript. We thank AERONET-OC's principal investigators, co-investigators, and their teams for their invaluable efforts in establishing, maintaining, and providing access to the data used in this study.

Conflicts of Interest: The authors declare no conflict of interest.

Appendix A GCOM-C/SGLI Characteristics

Table A1. Specifications of non-polarized bands of GCOM-C/SGLI Visible and Near Infrared Radiometer (SGLI-VNR), where SNR refers to the signal-to-noise ratio.

Bands	Central Wavelength (nm)	Bandwidth (nm)	Spatial Resolution (m)	SNR	Observation Width (km)
VNIR1	380	10	250	624–675	1150
VNIR2	412	10	250	786–826	1150
VNIR3	443	10	250	487–531	1150
VNIR4	490	10	250	858–870	1150
VNIR5	530	20	250	457–522	1150
VNIR6	565	20	250	1027–1064	1150
VNIR7	673.5	10	250	988–1088	1150
VNIR8	673.5	20	250	537–564	1150
VNIR9	763	8	1000	1592–1746	1150
VNIR10	868.5	20	250	470–510	1150
VNIR11	868.5	20	250	471–511	1150

Appendix B Trend and Seasonality

Figure A1. Trend and seasonality components of R_{rs} for five key bands (R_{rs}_412, R_{rs}_443, R_{rs}_490, R_{rs}_530, and R_{rs}_670) at the Socheongcho AERONET-OC site. The trend plots (left column) and seasonality plots (right column) illustrate the temporal behavior of remote sensing reflectance across G-Portal, JASMES, and AERONET-OC data.

Table A2. Trend and seasonality correlation coefficients between G-Portal (GP), JASMES (JS), and AERONET-OC (OC) for each band at the Socheongcho site.

	Trend Correlations			Seasonality Correlations		
Band	**GP<>JS**	**GP<>OC**	**JS<>OC**	**GP<>JS**	**GP<>OC**	**JS<>OC**
R_{rs}_412	0.43	0.45	0.45	−0.2	0.6	−0.19
R_{rs}_443	0.35	0.58	0.85	−0.02	0.87	0.12
R_{rs}_490	0.67	0.13	0.16	0.93	0.93	0.88
R_{rs}_530	−0.37	0.21	0.32	0.71	0.9	0.67
R_{rs}_670	0.56	−0.23	0.23	0.79	0.68	0.46

References

1. Gordon, H.R.; Morel, A. *Remote Assessment of Ocean Color for Interpretation of Satellite Visible Imagery: A Review*; Lecture Notes on Coastal and Estuarine Studies; Springer: Berlin/Heidelberg, Germany, 1983.
2. Morel, A.; Prieur, L. Analysis of variations in ocean color. *Limnol. Oceanogr.* **1977**, *22*, 709–722. [CrossRef]
3. Mobley, C.D. Optical Properties of Water. In *Light and Water: Radiative Transfer in Natural Waters*; Academic Press: Cambridge, MA, USA, 1994; pp. 60–144.
4. Gordon, H.R.; Clark, D.K. Clear water radiances for atmospheric correction of coastal zone color scanner imagery. *Appl. Opt.* **1981**, *20*, 4175–4180. [CrossRef]
5. Thuillier, G.; Hersé, M.; Foujols, T.; Peetermans, W.; Gillotay, D.; Simon, P.C.C.; Mandel, H.; Labs, D.; Foujols, T.; Peetermans, W.; et al. The solar spectral irradiance from 200 to 2400 nm as measured by the SOLSPEC spectrometer from the ATLAS and EURECA missions. *Sol. Phys.* **2003**, *214*, 1–22. [CrossRef]
6. Salem, S.I.; Higa, H.; Kim, H.; Kobayashi, H.; Oki, K.; Oki, T. Assessment of Chlorophyll-a Algorithms Considering Different Trophic Statuses and Optimal Bands. *Sensors* **2017**, *17*, 1746. [CrossRef]
7. Salah, M.; Higa, H.; Ishizaka, J.; Salem, S.I. 1D Convolutional Neural Network-based Chlorophyll-a Retrieval Algorithm for Sentinel-2 MultiSpectral Instrument in Various Trophic States. *Sens. Mater.* **2023**, *35*, 3743. [CrossRef]
8. Dekker, A.G. Detection of Optical Water Quality Parameters for Eutrophic Waters by High Resolution Remote Sensing. Ph.D. Thesis, Vrije Universiteit Amsterdam, Amsterdam, The Netherlands, 1993.
9. Yoder, J.A.; McClain, C.R.; Blanton, J.O.; Oeymay, L.-Y. Spatial scales in CZCS-chlorophyll imagery of the southeastern U.S. continental shelf. *Limnol. Oceanogr.* **1987**, *32*, 929–941. [CrossRef]
10. Lee, Z.; Carder, K.L.; Arnone, R.A. Deriving Inherent Optical Properties from Water Color: A Multiband Quasi-Analytical Algorithm for Optically Deep Waters. *Appl. Opt.* **2002**, *41*, 5755. [CrossRef]
11. Higa, H.; Ideno, R.; Salem, S.I.; Kobayashi, H. Uncertainty Analysis of Particle Backscattering Coefficient Measurement for Multiple Highly Turbid Water Areas in Ocean Color Remote Sensing. *Sens. Mater.* **2023**, *35*, 3807. [CrossRef]
12. Smith, M.E.; Bernard, S. Satellite Ocean Color Based Harmful Algal Bloom Indicators for Aquaculture Decision Support in Southern Benguela. *Front. Mar. Sci.* **2020**, *7*, 61. [CrossRef]
13. Higa, H.; Sugahara, S.; Salem, S.I.; Nakamura, Y.; Suzuki, T. An estimation method for blue tide distribution in Tokyo Bay based on sulfur concentrations using Geostationary Ocean Color Imager (GOCI). *Estuar. Coast. Shelf Sci.* **2020**, *235*, 106615. [CrossRef]
14. Murakami, H.; Ogata, K. GCOM-C/SGLI capability for coastal observation. In Proceedings of the SPIE Asia-Pacific Remote Sensing, Honolulu, HI, USA, 24–26 September 2018; Volume 10778, p. 107780D.
15. Cetinic, I.; McClain, C.R.; Werdell, P.J. *Pre-Aerosol, Clouds, and Ocean Ecosystem (PACE) Mission Science Definition Team Report*; NASA Goddard Space Flight Center: Washington, DC, USA, 2018.
16. Bonelli, A.G.; Loisel, H.; Jorge, D.S.F.; Mangin, A.; D'Andon, O.F.; Vantrepotte, V. A new method to estimate the dissolved organic carbon concentration from remote sensing in the global open ocean. *Remote Sens. Environ.* **2022**, *281*, 113227. [CrossRef]
17. Zhu, W.; Yu, Q. Inversion of Chromophoric Dissolved Organic Matter From EO-1 Hyperion Imagery for Turbid Estuarine and Coastal Waters. *IEEE Trans. Geosci. Remote Sens.* **2013**, *51*, 3286–3298. [CrossRef]
18. Mannino, A.; Russ, M.E.; Hooker, S.B. Algorithm development and validation for satellite-derived distributions of DOC and CDOM in the U.S. Middle Atlantic Bight. *J. Geophys. Res. Ocean.* **2008**, *113*, C07051. [CrossRef]
19. Schaaf, C.B.; Gao, F.; Strahler, A.H.; Lucht, W.; Li, X.; Tsang, T.; Strugnell, N.C.; Zhang, X.; Jin, Y.; Muller, J.-P.; et al. First operational BRDF, albedo nadir reflectance products from MODIS. *Remote Sens. Environ.* **2002**, *83*, 135–148. [CrossRef]
20. Wolfe, R.E.; Lin, G.; Nishihama, M.; Tewari, K.P.; Tilton, J.C.; Isaacman, A.R. Suomi NPP VIIRS prelaunch and on-orbit geometric calibration and characterization. *J. Geophys. Res. Atmos.* **2013**, *118*, 11508–11521. [CrossRef]
21. Isada, T.; Hooker, S.B.; Taniuchi, Y.; Suzuki, K. Evaluation of retrieving chlorophyll a concentration and colored dissolved organic matter absorption from satellite ocean color remote sensing in the coastal waters of Hokkaido, Japan. *J. Oceanogr.* **2022**, *78*, 263–276. [CrossRef]

22. Mobley, C.D.; Werdell, J.; Franz, B.; Ahmad, Z.; Bailey, S. *Atmospheric Correction for Satellite Ocean Color Radiometry*; NASA Goddard Space Flight Center: Washington, DC, USA, 2016.
23. Jaelani, L.M.; Matsushita, B.; Yang, W.; Fukushima, T. An improved atmospheric correction algorithm for applying MERIS data to very turbid inland waters. *Int. J. Appl. Earth Obs. Geoinf.* **2015**, *39*, 128–141. [CrossRef]
24. Soto, I.M.; Cannizzaro, J.; Muller-Karger, F.E.; Hu, C.; Wolny, J.; Goldgof, D. Evaluation and optimization of remote sensing techniques for detection of Karenia brevis blooms on the West Florida Shelf. *Remote Sens. Environ.* **2015**, *170*, 239–254. [CrossRef]
25. International Ocean Colour Coordinating Group (IOCCG). *Remote Sensing of Ocean Colour in Coastal, and Other Optically-Complex, Waters*; Reports of the International Ocean Colour Coordinating Group; Sathyendranath, S., Ed.; IOCCG: Dartmouth, NS, Canada, 2000; Volume 3.
26. Del Castillo, C.; Platnick, S.; Antoine, D. (Eds.) *Pre-Aerosol, Clouds, and Ocean Ecosystem (PACE) Mission Science Definition Team Report*; NASA Goddard Space Flight Center: Washington, DC, USA, 2012.
27. International Ocean Colour Coordinating Group (IOCCG). *Atmospheric Correction for Remotely-Sensed Ocean-Colour Products*; Reports of the International Ocean Colour Coordinating Group; Wang, M., Ed.; IOCCG: Dartmouth, NS, Canada, 2010; Volume 10.
28. Toratani, M.; Ogata, K.; Fukushima, H. SGLI Algorithm Theoretical Basis Document: Atmospheric Correction Algorithm for Ocean Color. Available online: https://suzaku.eorc.jaxa.jp/GCOM_C/data/ATBD/ver3/V3ATBD_O2AB_NWLR_toratani.pdf (accessed on 10 December 2024).
29. Murakami, H. *ATBD of GCOM-C Ocean Color Atmospheric Correction*; Archimer: Copenhagen, Denmark, 2020.
30. Salah, M.; Higa, H.; Ishizaka, J.; Salem, S.I. B1D-CNN: A Novel Convolution Neural Network-Based Chlorophyll-A Retrieval Algorithm for Sentinel-2 Data. In Proceedings of the International Geoscience and Remote Sensing Symposium (IGARSS), Pasadena, CA, USA, 16–21 July 2023; IEEE: New York City, NY, USA; Volume 2023, pp. 3950–3953.
31. Salem, S.I.; Strand, M.; Higa, H.; Kim, H.; Kazuhiro, K.; Oki, K.; Oki, T. Evaluation of MERIS Chlorophyll-a Retrieval Processors in a Complex Turbid Lake Kasumigaura over a 10-Year Mission. *Remote Sens.* **2017**, *9*, 1022. [CrossRef]
32. Gons, H.J.; Rijkeboer, M.; Ruddick, K.G. A chlorophyll-retrieval algorithm for satellite imagery (Medium Resolution Imaging Spectrometer) of inland and coastal waters. *J. Plankton Res.* **2002**, *24*, 947–951. [CrossRef]
33. Kishino, M.; Tanaka, A.; Ishizaka, J. Retrieval of Chlorophyll a, suspended solids, and colored dissolved organic matter in Tokyo Bay using ASTER data. *Remote Sens. Environ.* **2005**, *99*, 66–74. [CrossRef]
34. Dorji, P.; Fearns, P. A Quantitative Comparison of Total Suspended Sediment Algorithms: A Case Study of the Last Decade for MODIS and Landsat-Based Sensors. *Remote Sens.* **2016**, *8*, 810. [CrossRef]
35. Zibordi, G.; Holben, B.; Mélin, F.; D'Alimonte, D.; Berthon, J.-F.; Slutsker, I.; Giles, D. AERONET-OC: An overview. *Can. J. Remote Sens.* **2010**, *36*, 488–497. [CrossRef]
36. Zibordi, G.; Berthon, J.-F.; Melin, F.; D'Alimonte, D.; Kaitala, S. Validation of satellite ocean color primary products at optically complex coastal sites: Northern Adriatic Sea, Northern Baltic Proper and Gulf of Finland. *Remote Sens. Environ.* **2009**, *113*, 2574–2591. [CrossRef]
37. Zibordi, G.; Mélin, F.; Berthon, J.-F.; Holben, B.; Slutsker, I.; Giles, D.; D'Alimonte, D.; Vandemark, D.; Feng, H.; Schuster, G.; et al. AERONET-OC: A Network for the Validation of Ocean Color Primary Products. *J. Atmos. Ocean. Technol.* **2009**, *26*, 1634–1651. [CrossRef]
38. Cox, C.; Munk, W. Measurement of the roughness of the sea surface from photographs of the sun's glitter. *Josa* **1954**, *44*, 838–850. [CrossRef]
39. Frouin, R.; Deschamps, P.-Y.; Gross-Colzy, L.; Murakami, H.; Nakajima, T.Y. Retrieval of chlorophyll-a concentration via linear combination of ADEOS-II Global Imager data. *J. Oceanogr.* **2006**, *62*, 331–337. [CrossRef]
40. Morel, A.; Gentili, B. Diffuse reflectance of oceanic waters. III. Implication of bidirectionality for the remote-sensing problem. *Appl. Opt.* **1996**, *35*, 4850–4862. [CrossRef] [PubMed]
41. Hu, C.; Feng, L.; Lee, Z.; Franz, B.A.; Bailey, S.W.; Werdell, P.J.; Proctor, C.W. Improving Satellite Global Chlorophyll a Data Products Through Algorithm Refinement and Data Recovery. *J. Geophys. Res. Ocean.* **2019**, *124*, 1524–1543. [CrossRef]
42. Hu, C.; Lee, Z.; Franz, B. Chlorophyll a algorithms for oligotrophic oceans: A novel approach based on three-band reflectance difference. *J. Geophys. Res. Ocean.* **2012**, *117*, C01011. [CrossRef]
43. O'Reilly, J.E.; Maritorena, S.; Siegel, D.A.; O'Brien, M.C.; Toole, D.; Mitchell, B.G.; Kahru, M.; Chavez, F.P.; Strutton, P.; Cota, G.F. Ocean color chlorophyll a algorithms for SeaWiFS, OC2, and OC4: Version 4. In *SeaWiFS Postlaunch Calibration and Validation Analyses, Part 3*; NASA Goddard Space Flight Center: Washington, DC, USA, 2000; Volume 3, pp. 9–23.
44. Werdell, P.J.; Bailey, S.W. An improved in-situ bio-optical data set for ocean color algorithm development and satellite data product validation. *Remote Sens. Environ.* **2005**, *98*, 122–140. [CrossRef]
45. Toratani, M. *SGLI Algorithm Theoretical Basis Document: Total Suspended Matter Concentration*; Tokai University: Tokyo, Japan, 2021.
46. Morel, A.; Antoine, D.; Gentili, B. Bidirectional reflectance of oceanic waters: Accounting for Raman emission and varying particle scattering phase function. *Appl. Opt.* **2002**, *41*, 6289–6306. [CrossRef]

47. Lee, Z.P.; Du, K.; Voss, K.J.; Zibordi, G.; Lubac, B.; Arnone, R.; Weidemann, A. An inherent-optical-property-centered approach to correct the angular effects in water-leaving radiance. *Appl. Opt.* **2011**, *50*, 3155–3167. [CrossRef] [PubMed]
48. Gleason, A.C.R.; Voss, K.J.; Gordon, H.R.; Twardowski, M.; Sullivan, J.; Trees, C.; Weidemann, A.; Berthon, J.-F.; Clark, D.; Lee, Z.-P. Detailed validation of the bidirectional effect in various Case I and Case II waters. *Opt. Express* **2012**, *20*, 7630–7645. [CrossRef]
49. Salem, S.I.; Higa, H.; Ishizaka, J.; Pahlevan, N.; Oki, K. Spectral band-shifting of multispectral remote-sensing reflectance products: Insights for matchup and cross-mission consistency assessments. *Remote Sens. Environ.* **2023**, *299*, 113846. [CrossRef]
50. Melin, F.; Sclep, G. Band shifting for ocean color multi-spectral reflectance data. *Opt. Express* **2015**, *23*, 2262–2279. [CrossRef] [PubMed]
51. Lehmann, M.K.; Gurlin, D.; Pahlevan, N.; Alikas, K.; Anstee, J.; Balasubramanian, S.V.; Barbosa, C.C.F.; Binding, C.; Bracher, A.; Bresciani, M.; et al. GLORIA—A globally representative hyperspectral in situ dataset for optical sensing of water quality. *Sci. Data* **2023**, *10*, 100. [CrossRef] [PubMed]
52. Lehmann, M.K.; Gurlin, D.; Pahlevan, N.; Alikas, K.; Anstee, J.M.; Balasubramanian, S.V.; Barbosa, C.C.F.; Binding, C.; Bracher, A.; Bresciani, M.; et al. *GLORIA—A Global Dataset of Remote Sensing Reflectance and Water Quality from Inland and Coastal Waters*; PANGAEA: Bremen, Germany, 2022.
53. Mitchell, B.G.; Kahru, M.; Wieland, J.; Stramska, M.; Mueller, J.L. Determination of spectral absorption coefficients of particles, dissolved material and phytoplankton for discrete water samples. In *Ocean Optics Protocols for Satellite Ocean Color Sensor Validation*; NASA Goddard Space Flight Center: Washington, DC, USA, 2002; Volume 3, pp. 231–257.
54. Mobley, C.D. Estimation of the Remote-Sensing Reflectance from Above-Surface Measurements. *Appl. Opt.* **1999**, *38*, 7442. [CrossRef]
55. Suzuki, R.; Ishimaru, T. An improved method for the determination of phytoplankton chlorophyll using N, N-dimethylformamide. *J. Oceanogr. Soc. Jpn.* **1990**, *46*, 190–194. [CrossRef]
56. American Public Health Association. *Standard Methods for the Examination of Water and Wastewater*; American Public Health Association: Washington, DC, USA, 2005; ISBN 0875530478 9780875530475.
57. Barnes, B.B.; Cannizzaro, J.P.; English, D.C.; Hu, C. Validation of VIIRS and MODIS reflectance data in coastal and oceanic waters: An assessment of methods. *Remote Sens. Environ.* **2019**, *220*, 110–123. [CrossRef]
58. Matthews, M.W.; Bernard, S.; Robertson, L. An algorithm for detecting trophic status (chlorophyll-a), cyanobacterial-dominance, surface scums and floating vegetation in inland and coastal waters. *Remote Sens. Environ.* **2012**, *124*, 637–652. [CrossRef]
59. Theil, H. *Henri Theil's Contributions to Economics and Econometrics*; Kluwer Academic Publishers: Dordrecht, The Netherlands, 1992; ISBN 0792316649.
60. Sen, P.K. Estimates of the Regression Coefficient Based on Kendall's Tau. *J. Am. Stat. Assoc.* **1968**, *63*, 1379–1389. [CrossRef]
61. Osterholz, H.; Burmeister, C.; Busch, S.; Dierken, M.; Frazão, H.C.; Hansen, R.; Jeschek, J.; Kremp, A.; Kreuzer, L.; Sadkowiak, B.; et al. Nearshore Dissolved and Particulate Organic Matter Dynamics in the Southwestern Baltic Sea: Environmental Drivers and Time Series Analysis (2010–2020). *Front. Mar. Sci.* **2021**, *8*, 795028. [CrossRef]
62. Glover, D.M.; Jenkins, W.J.; Doney, S.C. *Modeling Methods for Marine Science*; Cambridge University Press: Cambridge, UK, 2011; ISBN 1139500716.
63. Brewin, R.J.W.; Sathyendranath, S.; Müller, D.; Brockmann, C.; Deschamps, P.-Y.; Devred, E.; Doerffer, R.; Fomferra, N.; Franz, B.; Grant, M.; et al. The Ocean Colour Climate Change Initiative: III. A round-robin comparison on in-water bio-optical algorithms. *Remote Sens. Environ.* **2015**, *162*, 271–294. [CrossRef]
64. Müller, D.; Krasemann, H.; Brewin, R.J.W.; Brockmann, C.; Deschamps, P.-Y.; Doerffer, R.; Fomferra, N.; Franz, B.A.; Grant, M.G.; Groom, S.B.; et al. The Ocean Colour Climate Change Initiative: I. A methodology for assessing atmospheric correction processors based on in-situ measurements. *Remote Sens. Environ.* **2015**, *162*, 242–256. [CrossRef]
65. Botygin, I.; Sherstneva, A.; Sherstnev, V. *Solving Some Problems of Predictive Analytics for Time Series Data BT—Software Engineering Perspectives in Systems*; Silhavy, R., Ed.; Springer International Publishing: Cham, Switzerland, 2022; pp. 382–391.
66. Toratani, M.; Ogata, K.; Fukushima, H. *Atmospheric Correction Algorithm for Ocean Color*; Tokai University: Tokyo, Japan, 2020.
67. Zhou, L.; Roberts, D.A.; Ma, W.; Zhang, H.; Tang, L. Estimation of higher chlorophylla concentrations using field spectral measurement and HJ-1A hyperspectral satellite data in Dianshan Lake, China. *ISPRS J. Photogramm. Remote Sens.* **2014**, *88*, 41–47. [CrossRef]
68. Nobileau, D.; Antoine, D. Detection of blue-absorbing aerosols using near infrared and visible (ocean color) remote sensing observations. *Remote Sens. Environ.* **2005**, *95*, 368–387. [CrossRef]
69. Kowalczuk, P.; Olszewski, J.; Darecki, M.; Kaczmarek, S. Empirical relationships between coloured dissolved organic matter (CDOM) absorption and apparent optical properties in Baltic Sea waters. *Int. J. Remote Sens.* **2007**, *26*, 345–370. [CrossRef]
70. Vanhellemont, Q.; Ruddick, K. Atmospheric correction of metre-scale optical satellite data for inland and coastal water applications. *Remote Sens. Environ.* **2018**, *216*, 586–597. [CrossRef]
71. Schroeder, T.; Schaale, M.; Fischer, J. Retrieval of atmospheric and oceanic properties from MERIS measurements: A new Case-2 water processor for BEAM. *Int. J. Remote Sens.* **2007**, *28*, 5627–5632. [CrossRef]

72. Bai, R.; He, X.; Bai, Y.; Gong, F.; Zhu, Q.; Wang, D.; Li, T. Atmospheric correction algorithm based on the interpolation of ultraviolet and shortwave infrared bands. *Opt. Express* **2023**, *31*, 6805–6826. [CrossRef] [PubMed]
73. Sekiguchi, M.; Shi, C.; Hashimoto, M.; Nakajima, T. Analysis and validation of ocean color and aerosol properties over coastal regions from SGLI based on a simultaneous method. *J. Oceanogr.* **2022**, *78*, 229–243. [CrossRef]
74. Wang, Y.; Lee, Z.; Wei, J.; Shang, S.; Wang, M.; Lai, W. Extending satellite ocean color remote sensing to the near-blue ultraviolet bands. *Remote Sens. Environ.* **2021**, *253*, 112228. [CrossRef]
75. Gilerson, A.A.; Gitelson, A.A.; Zhou, J.; Gurlin, D.; Moses, W.; Ioannou, I.; Ahmed, S.A. Algorithms for remote estimation of chlorophyll-a in coastal and inland waters using red and near infrared bands. *Opt. Express* **2010**, *18*, 24109–24125. [CrossRef] [PubMed]
76. Gower, J.F.R.; Doerffer, R.; Borstad, G.A. Interpretation of the 685nm peak in water-leaving radiance spectra in terms of fluorescence, absorption and scattering, and its observation by MERIS. *Int. J. Remote Sens.* **1999**, *20*, 1771–1786. [CrossRef]
77. Aurin, D.; Mannino, A.; Lary, D.J. Remote Sensing of CDOM, CDOM Spectral Slope, and Dissolved Organic Carbon in the Global Ocean. *Appl. Sci.* **2018**, *8*, 2687. [CrossRef]
78. Le, C.; Hu, C.; Cannizzaro, J.; English, D.; Muller-Karger, F.; Lee, Z. Evaluation of chlorophyll-a remote sensing algorithms for an optically complex estuary. *Remote Sens. Environ.* **2013**, *129*, 75–89. [CrossRef]
79. Zibordi, G.; Mélin, F. An evaluation of marine regions relevant for ocean color system vicarious calibration. *Remote Sens. Environ.* **2017**, *190*, 122–136. [CrossRef]